
Metriplector: From Field Theory to Neural Architecture

Dan Oprisa* Peter Toth*
Spheroid Labs*

Abstract

We present **Metriplector**, a neural architecture primitive in which the input configures an abstract physical system—fields, sources, and operators—and the dynamics of that system *is* the computation. Multiple fields evolve via coupled metriplectic dynamics, and the stress-energy tensor $T^{\mu\nu}$, derived from Noether’s theorem, provides the readout. The metriplectic formulation admits a natural spectrum of instantiations: the dissipative branch alone yields a screened Poisson equation solved exactly via conjugate gradient; activating the full structure—including the antisymmetric Poisson bracket—gives field dynamics for image recognition and language modeling. We evaluate Metriplector across four domains, each using a task-specific architecture built from this shared primitive with progressively richer physics: **F1 = 1.0** on maze pathfinding, generalizing from 15×15 training grids to unseen 39×39 grids; **97.2%** exact Sudoku solve rate with zero structural injection; **81.03%** on CIFAR-100 with 2.26M parameters; and **1.182 bits/byte** on language modeling with $3.6 \times$ fewer training tokens than a GPT baseline.

1 Introduction

Physics offers a rich source of principled structures for computation: conservation laws that guarantee what information is preserved, variational principles that determine how systems evolve, and symmetry theorems that connect structure to observables. These are not heuristics—they are exact, composable, and universal. If they can be instantiated as trainable architecture primitives, the physical structure itself carries part of the computational load, potentially reducing the capacity needed to solve a problem. The long-term vision is a *standard model* of neural computation—a unified framework of physics-grounded primitives, each derived from a different physical principle, that can be composed the way physical theories are composed to describe nature.

This paper takes a step in that direction: *the energy landscape is the program*. The input to a computation configures an abstract physical system—its boundary conditions, source terms, conductances, and advection operators. The dynamics of that system *is* the computation: fields ψ evolve under the metriplectic (GENERIC) equation, and the stress-energy tensor $T^{\mu\nu}$ —derived from Noether’s theorem—provides the readout. A central finding is that what appear to be domain-specific architectures for recognition (CIFAR-100) and reasoning (Sudoku) are in fact *the same physics*: both read off $T^{\mu\nu}$ from evolved fields, and the multigrid object layer that discovers Sudoku boxes performs learned coarse-graining analogous to block-spin methods [Kadanoff, 1966].

We develop this idea from first principles. We begin with the physics: Lagrangian and Hamiltonian mechanics, the GENERIC framework [Grmela & Öttinger, 1997, Öttinger, 2005] that unifies reversible and irreversible dynamics in a single equation, and Noether’s theorem [Noether, 1918] connecting symmetries to conservation laws (Section 2). We then show how residual neural network layers can be understood as dynamics on energy landscapes, and how metriplectic structure provides conservation guarantees that general-purpose architectures lack.

*spheroid.ai. *Equal contribution. Correspondence: {dan, peter}@spheroid.ai

Metriplector: K fields evolve via metriplectic dynamics, readout via $\nabla\psi\otimes\nabla\psi$ stress-energy tensor

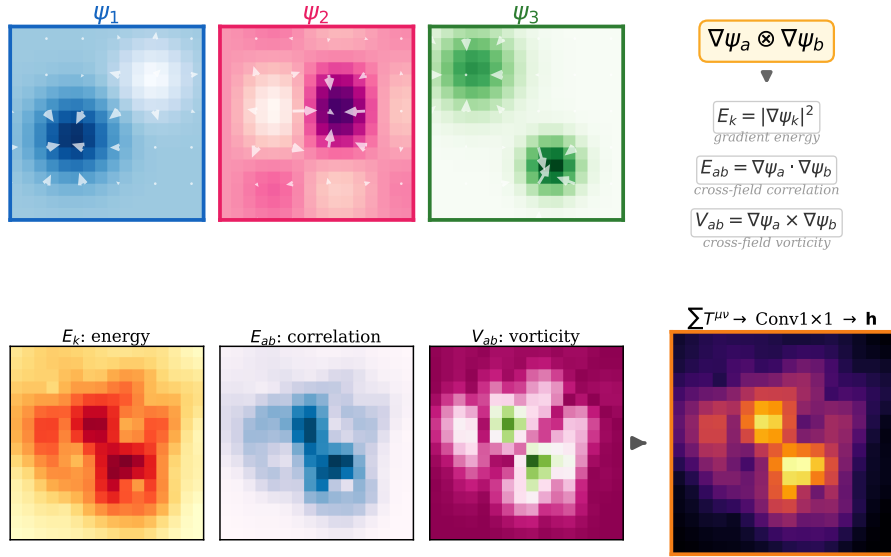


Figure 1: **Metriplector field interaction.** *Top:* K fields ψ_k evolve via metriplectic dynamics over the spatial grid (gradient arrows show $\nabla\psi_k$); the outer product $\nabla\psi_a \otimes \nabla\psi_b$ yields three stress-energy components. *Bottom:* per-field gradient energy $E_k = |\nabla\psi_k|^2$, cross-field correlation $E_{ab} = \nabla\psi_a \cdot \nabla\psi_b$, and vorticity $V_{ab} = \nabla\psi_a \times \nabla\psi_b$, summed and projected via $\text{Conv}1 \times 1$ into \mathbf{h} . Shown for $K=3$; the full model uses $K=32$.

From this foundation, we distill **Metriplector**: a physics-native architecture primitive that instantiates the metriplectic equation differently for each domain (Section 3). In its simplest form, the metriplectic equation reduces to a screened Poisson equation on a graph:

$$(L_W + \Lambda)\psi = \mathbf{b}, \quad (1)$$

where L_W is a learned weighted graph Laplacian, Λ is per-node damping, and \mathbf{b} is a learned source vector. For spatial reasoning, this is solved exactly via conjugate gradient; for language modeling, the causal structure allows $O(N \log N)$ parallel scan solutions; for recognition, the full metriplectic dynamics—including the antisymmetric Poisson bracket—is evolved via Euler integration.

Contributions.

1. A **physics-native architecture primitive** grounded in the metriplectic framework, in which the input configures an abstract physical system and the dynamics is the computation (Section 2).
2. The **stress-energy tensor $T^{\mu\nu}$ as a principled readout**: we show that the conserved quantity from Noether’s theorem provides the most effective feature extraction from evolved fields, outperforming heuristic alternatives by 0.6–2.6 accuracy points on CIFAR-100 (Section 3.5). The same readout (diagonal $T^{\mu\nu}$) underlies the Sudoku instantiation, unifying recognition and constraint satisfaction under a single physics (Section 5).
3. A **metriplectic spectrum** of instantiations with progressively richer dynamics: the dissipative branch alone (screened Poisson, solved exactly via CG) suffices for spatial reasoning; the full metriplectic structure (Poisson bracket + metric tensor) is needed for recognition; and a causal variant enables language modeling (Section 3).
4. Two **transferable design principles** validated by ablation: the *operator-from-input* separation, where the representation \mathbf{h} defines the physics and the fields ψ are the solution (removing it costs 14.3 accuracy points); and *zero structural injection*, where task structure is discovered from data rather than encoded in the graph topology (Section 5).

5. **Cross-domain experimental validation:** 81.03% on CIFAR-100 (2.26M params); 97.2% exact Sudoku solve (120K params, zero injection); 1.182 BPB on language modeling (3.6× fewer tokens than GPT); F1 = 1.0 on maze pathfinding (43.8K params) with generalization to unseen 39×39 grids (Section 4).

2 From Physics to Neural Computation

This section develops the mathematical structures that Metriplector builds on: variational mechanics, the GENERIC framework, Noether’s theorem, and the algebraic structure of the Poisson bracket.

2.1 From Lagrangians to Hamiltonians

The foundation of all physics is the *principle of stationary action*. A physical system with generalised coordinates q and velocities \dot{q} is described by a Lagrangian $\mathcal{L}(q, \dot{q}, t) = T - V$, where T is kinetic and V potential energy. The true trajectory extremises the action functional:

$$\mathcal{A}[q] = \int_{t_0}^{t_1} \mathcal{L}(q, \dot{q}, t) dt, \quad \delta\mathcal{A} = 0 \implies \frac{d}{dt} \frac{\partial \mathcal{L}}{\partial \dot{q}_i} - \frac{\partial \mathcal{L}}{\partial q_i} = 0. \quad (2)$$

These are the Euler–Lagrange equations—the most general statement of classical dynamics.

The *Hamiltonian formulation* reformulates this in terms of positions q and conjugate momenta $p_i = \partial \mathcal{L} / \partial \dot{q}_i$:

$$H(q, p) = \sum_i p_i \dot{q}_i - \mathcal{L}, \quad \dot{q}_i = \frac{\partial H}{\partial p_i}, \quad \dot{p}_i = -\frac{\partial H}{\partial q_i}. \quad (3)$$

Hamilton’s equations are equivalent to the Euler–Lagrange equations but reveal a deeper structure: the *symplectic structure* of phase space. The state $z = (q, p)$ evolves as $\dot{z} = J_0 \nabla H$, where $J_0 = \begin{pmatrix} 0 & I \\ -I & 0 \end{pmatrix}$ is the canonical symplectic matrix—skew-symmetric by construction, guaranteeing exact energy conservation:

$$\frac{dH}{dt} = \nabla H^\top J_0 \nabla H = 0. \quad (4)$$

This is the key insight for neural architecture design: *the dynamics is determined entirely by the energy landscape H and the structure matrix J_0* . The energy landscape encodes *what* the system knows; the structure matrix encodes *how* information flows. Neural networks that respect this separation inherit the stability, conservation, and interpretability of Hamiltonian mechanics.

From particles to fields. When the degrees of freedom are continuous—a vibrating membrane, an electromagnetic field, a neural feature map—the Lagrangian becomes a functional over fields $\psi(x, t)$:

$$\mathcal{A}[\psi] = \int \mathcal{L}(\psi, \nabla \psi, \partial_t \psi) d^n x dt. \quad (5)$$

The Euler–Lagrange equations become partial differential equations. A 2D convolutional feature map at layer ℓ is precisely such a field: $\psi^{(\ell)}(x, y)$ is a function on a spatial grid, and the convolution kernel defines the local interaction Lagrangian. Metriplector makes this analogy literal: it evolves K physics fields ψ_1, \dots, ψ_K on a spatial grid under dynamics derived from a Hamiltonian energy functional.

2.2 Every Physical System in One Equation

The GENERIC (General Equation for Non-Equilibrium Reversible-Irreversible Coupling) framework [Gmela & Öttinger, 1997, Öttinger, 2005] unifies all of classical physics:

$$\dot{z} = \underbrace{L(z) \cdot \nabla E(z)}_{\text{reversible (Hamiltonian)}} + \underbrace{M(z) \cdot \nabla S(z)}_{\text{irreversible (dissipative)}}, \quad (6)$$

with degeneracy conditions:

$$\begin{aligned} M \cdot \nabla E &= 0 && \text{(dissipation cannot change energy),} \\ L \cdot \nabla S &= 0 && \text{(Hamiltonian dynamics cannot produce entropy).} \end{aligned} \quad (7)$$

The Hamiltonian channel ($L \cdot \nabla E$) describes reversible dynamics: L is skew-symmetric, so $dE/dt = \nabla E^\top L \nabla E = 0$ —energy is exactly conserved. The dissipative channel ($M \cdot \nabla S$) describes irreversible dynamics: M is symmetric positive semi-definite, so $dS/dt = \nabla S^\top M \nabla S \geq 0$ —entropy never decreases. Together, these structural properties are *built into the architecture*, not learned from data.

2.3 Metriplector as Dissipative GENERIC

Each Poisson solve in Metriplector finds the steady state of the dissipative branch ($L = 0$):

$$0 = M \cdot \nabla S(\psi) \implies (L_W + \Lambda)\psi = \mathbf{b}, \quad (8)$$

where the Onsager matrix $M = L_W + \Lambda$ is SPD (satisfying the Onsager reciprocal relations [Onsager, 1931]) and the entropy functional is $S(\psi) = -\frac{1}{2}\psi^\top (L_W + \Lambda)\psi + \mathbf{b}^\top \psi$.

The Poisson solution minimizes the screened Dirichlet energy:

$$\mathcal{E}_{\text{Dir}}(\psi) = \frac{1}{2} \sum_{(i,j) \in E} w_{ij}(\psi_i - \psi_j)^2 + \frac{1}{2} \sum_i \Lambda_i \psi_i^2 - \sum_i b_i \psi_i. \quad (9)$$

Since the Hessian $L_W + \Lambda$ is SPD (Proposition 2), the critical point is the unique global minimum—the physical equilibrium.

2.4 Full Metriplectic Dynamics for Recognition

For reasoning tasks (maze, Sudoku), the dissipative branch alone suffices: the equilibrium of the screened Poisson equation encodes the answer, and the Hamiltonian channel plays no role ($L = 0$). For recognition (CIFAR-100), both branches of the GENERIC equation (6) are active:

$$\psi \leftarrow \psi + \Delta t \left[\underbrace{-\sigma \cdot \nabla^2 \psi}_{\text{diffusion } (M)} + \underbrace{\alpha \cdot J_{\text{anti}} \psi}_{\text{advection } (L)} - \underbrace{\gamma \psi}_{\text{damping}} + \underbrace{\mathbf{s}}_{\text{source}} \right], \quad (10)$$

where J is a raw learned $K \times K$ matrix and $J_{\text{anti}} = J - J^\top$ is its antisymmetrization, yielding a skew-symmetric Poisson tensor that mediates cross-field coupling. Throughout the paper, references to “ J ” in the context of the Poisson bracket refer to this antisymmetrized form J_{anti} unless otherwise noted. ∇^2 is a depthwise convolution approximating the Laplacian on the image grid, and the coefficients $\sigma, \alpha, \gamma, \mathbf{s}$ are produced from the representation \mathbf{h} via $\text{Conv}1 \times 1$ projections.

The Poisson bracket J_{anti} enables *advection*—it rotates information between the K fields without dissipating it. The metric tensor M (diffusion + damping) enables *spatial smoothing*—spreading information across the image grid and damping irrelevant variation. Recognition requires both: spatial smoothing builds invariance to local perturbations, while cross-field advection constructs the feature interactions needed for fine-grained class discrimination.

This creates a spectrum of metriplectic instantiations (Figure 2):

Domain	Active channels	Solver	Dynamics
Maze	M only	Exact CG	Equilibrium
Sudoku	M only	Exact CG	Iterated equilibrium
CIFAR-100	$M + L$	Euler steps	Progressive evolution
Language	M only (causal)	Parallel scan	Causal propagation

2.5 Symmetries and Conservation Laws

Noether’s theorem [Noether, 1918] connects symmetries to conserved currents: every continuous symmetry of the action \mathcal{A} yields a conserved current.

Theorem 1 (Noether’s theorem, 1918). *If the action $\mathcal{A}[\psi] = \int \mathcal{L}(\psi, \partial_\mu \psi) d^n x$ is invariant under a continuous one-parameter family of transformations $\psi \rightarrow \psi + \epsilon \delta \psi$, then the current*

$$j^\mu = \frac{\partial \mathcal{L}}{\partial(\partial_\mu \psi_a)} \delta \psi_a - \left(\frac{\partial \mathcal{L}}{\partial(\partial_\mu \psi_a)} \partial_\nu \psi_a - \delta_\nu^\mu \mathcal{L} \right) \delta x^\nu \quad (11)$$

is conserved: $\partial_\mu j^\mu = 0$.

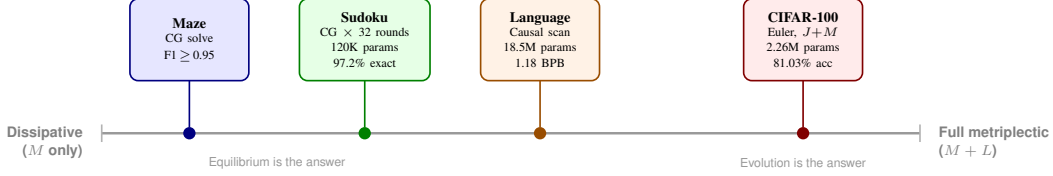


Figure 2: **The metriplectic spectrum.** All four domains instantiate the same GENERIC equation. Maze and Sudoku use only the dissipative branch (M), solved at equilibrium via CG. Language uses causal dissipation via scan. CIFAR-100 activates full metriplectic structure ($M+L$) via Euler integration.

For Metriplector, Noether’s theorem provides both the theoretical justification for the architecture and the optimal readout features:

Symmetry	Conserved quantity	Role in Metriplector
Spatial translation	Stress-energy tensor $T_{\mu\nu}$	Readout features ($\nabla\psi \times \nabla\psi$)
Spatial rotation	Angular momentum L_z	Noether readout ($x p_y - y p_x$)
Scale invariance	Dilation current D	Noether readout ($x p_x + y p_y$)
Time translation	Energy E	Conserved by Poisson bracket J
Phase rotation	Charge / particle number	Conserved charges of J

The stress-energy tensor deserves special attention. For a system of K fields ψ_1, \dots, ψ_K with Lagrangian density $\mathcal{L} = \frac{1}{2} \sum_a |\nabla\psi_a|^2 - V(\psi)$, spatial translation invariance yields:

$$T_{ab}^{ij} = \partial_i \psi_a \cdot \partial_j \psi_b, \quad i, j \in \{x, y\}, \quad a, b \in \{1, \dots, K\}. \quad (12)$$

The diagonal terms T_{aa}^{ii} are the energy density of field a in direction i ; the off-diagonal terms encode cross-field correlations. This is precisely the readout that Metriplector uses for CIFAR-100 classification (Section 3.5)—not as a heuristic, but as the *natural observable* dictated by the symmetries of the dynamics. Section 3.5 shows that this physics-derived readout yields 0.6–2.6 accuracy points above heuristic alternatives.

2.6 Algebraic Structure: Lie Groups and the Poisson Bracket

The Poisson bracket in GENERIC has a deep algebraic origin: it is a Lie bracket on the space of observables [Arnol’d, 1989, Marsden & Ratiu, 1999].

Lie algebra of observables. For any two observables F, G on phase space, the Poisson bracket

$$\{F, G\} = \sum_i \left(\frac{\partial F}{\partial q_i} \frac{\partial G}{\partial p_i} - \frac{\partial F}{\partial p_i} \frac{\partial G}{\partial q_i} \right) = (\nabla F)^\top J_0 \nabla G \quad (13)$$

satisfies skew-symmetry ($\{F, G\} = -\{G, F\}$), the Jacobi identity ($\{F, \{G, H\}\} + \text{cyclic} = 0$), and the Leibniz rule. These are exactly the axioms of a Lie algebra. A function C satisfying $\{C, H\} = 0$ for all H is a *Casimir invariant*—conserved by *any* Hamiltonian dynamics, not just a specific one. In Metriplector, the learned Poisson tensor J defines a Lie algebra on the K -field space. The skew-symmetry of J guarantees energy conservation ($dH/dt = 0$ along the Hamiltonian flow); whether the architecture additionally learns non-trivial Casimir invariants remains an open question for future investigation.

Symmetric and antisymmetric decomposition. Any bilinear interaction between field components ψ_a and ψ_b decomposes into a symmetric part and an antisymmetric part. In the metriplectic framework, these have distinct physical roles:

- **Symmetric** ($M_{ab} = M_{ba}$, positive semi-definite): governs the *metric bracket*—dissipation, diffusion, irreversible relaxation. The Onsager reciprocal relations [Onsager, 1931] require this symmetry.

- **Antisymmetric** ($J_{ab} = -J_{ba}$): governs the *Poisson bracket*—advection, rotation, reversible dynamics. The skew-symmetry guarantees exact energy conservation along the Hamiltonian flow.

The metriplectic equation $\dot{z} = (M + L)\nabla E$ decomposes the dynamics into these two complementary channels by construction. In K -dimensional field space, the Poisson bracket J couples all K fields via a learned $K \times K$ antisymmetric matrix ($J_{\text{anti}} = J - J^\top$), while the stress-energy readout extracts all K^2 pairwise interactions: K diagonal (gradient energy), $K(K-1)/2$ symmetric (cross-field correlation), and $K(K-1)/2$ antisymmetric (vorticity). For $K=32$, this yields 1,024 physics features—a complete decomposition of the inter-field coupling space. The K -field bottleneck (projecting from $D=128$ representation space to $K=32$ physics space) makes this completeness tractable.

2.7 Neural Architectures as Hamiltonian Systems

Residual neural network layers can be analysed as dynamics on energy landscapes. The differences between architectures reduce to (i) the Hamiltonian H , (ii) the dynamics (dissipative, conservative, or both), and (iii) the spatial coupling.

The universal form. Any residual layer $\psi_{\text{new}} = \psi + \Delta\psi$ can be analysed by asking: is $\Delta\psi$ the gradient of some energy function $H(\psi)$? If $\Delta\psi = -\nabla H$, the layer performs gradient descent on H . If $\Delta\psi = J \cdot \nabla H$ for skew-symmetric J , the layer performs Hamiltonian flow. If $\Delta\psi = (M + J)\nabla H$, it performs metriplectic dynamics. The Hamiltonian H encodes *what good features look like*; the dynamics encodes *how to get there*.

Transformer attention as a dissipative system. Self-attention computes $\Delta\mathbf{h}_i = \sum_j \text{softmax}(Q_i \cdot K_j / \sqrt{d})_j \cdot V_j$. This is the gradient of a LogSumExp energy:

$$H_{\text{attn}}(\mathbf{h}) = - \sum_i \log \sum_j \exp(\mathbf{h}_i^\top W_Q W_K^\top \mathbf{h}_j / \sqrt{d}), \quad (14)$$

whose gradient is precisely the softmax-weighted value aggregation (cf. modern Hopfield networks [Ramsauer et al., 2021]). The MLP block adds a second energy $H_{\text{MLP}} = - \sum_i \|\text{ReLU}(W_{\text{up}} \mathbf{h}_i)\|^2$. Both are *purely dissipative*: every layer descends its energy landscape. There is no conservative component—energy is not preserved across layers.

The attention Hamiltonian is *nonlinear* (LogSumExp \rightarrow softmax), which gives transformers their expressiveness. The softmax creates competitive dynamics: the most similar token dominates, others are suppressed. This winner-take-all behaviour is the source of attention’s power—and it arises from the *shape* of the energy landscape, not from the dynamics.

Metriplector as a designed metriplectic system. Metriplector operates in a compressed field space ($K=32$) where the complete set of pairwise field interactions is tractable. During dynamics, J couples all K fields via matrix multiply; at readout, the stress-energy tensor $T^{\mu\nu}$ extracts all $K^2 = 1,024$ pairwise features (K diagonal + $K(K-1)/2$ symmetric + $K(K-1)/2$ antisymmetric). The symmetric-antisymmetric decomposition is preserved by construction: the metric tensor M (symmetric, PSD) governs diffusion, while the Poisson bracket J (skew-symmetric) governs advection. These roles are enforced architecturally, not learned.

The key structural differences between attention and Metriplector are summarised in Table 1.

The comparison reveals a design space along two axes: the *expressiveness* of the Hamiltonian (how nonlinear is H ?) and the *structure* of the dynamics (how much of the metriplectic decomposition is preserved?). Attention has the most expressive H (LogSumExp) with purely dissipative dynamics. Metriplector preserves the full metriplectic structure while drawing its nonlinearity from the physics itself—the composition of metriplectic evolution steps across layers, modulated by content-dependent operators.

By construction, the composition of metriplectic evolution steps across layers can approximate any port-Hamiltonian system with dissipation while preserving structural laws—the antisymmetric Poisson bracket conserves energy exactly, and the symmetric positive-semidefinite metric tensor guarantees entropy production. Information propagation on the latent graph is bounded: the screened

Table 1: **Attention vs. Metriplector as dynamical systems.** Each layer’s update $\Delta\psi$ can be decomposed into dynamics type (how it moves on the energy landscape) and Hamiltonian type (what the landscape looks like). D = representation dimension, K = field dimension, N = spatial positions.

	Attention	Metriplector
Dynamics	Pure dissipation (∇H only)	Designed metriplectic ($M+J$)
Hamiltonian	LogSumExp (nonlinear)	Spatial (quadratic) + stress-energy
Spatial coupling	Global (all-to-all in standard form)	Local, $O(9N)$ DWConv 3×3
Channel mixing	MLP ($O(D^2)$)	Complete J + stress-energy ($O(K^2)$)
Conservation	None	Energy conservation by antisymmetric J
Cross-field coverage	—	All $K(K-1)/2$ pairs

Laplacian’s exponential decay implies that recurrent rounds are necessary and sufficient for long-range reasoning, analogous to the Lieb-Robinson bound in lattice systems [Lieb & Robinson, 1972, Nachtergaele & Sims, 2006].

3 The Metriplector Architecture

3.1 Dissipative Branch: Screened Poisson on Graphs

The dissipative branch of the GENERIC equation, shared across spatial reasoning domains, takes the form:

$$(L_W + \text{diag}(\Lambda_k))\psi_k = \mathbf{b}_k, \quad k = 1, \dots, K, \quad (15)$$

where L_W is the weighted graph Laplacian with learned edge conductances:

$$w_{ij} = \text{softplus}(\mathbf{h}_i^\top W_{\text{sym}} \mathbf{h}_j), \quad W_{\text{sym}} = \text{ReLU}\left(\frac{1}{2}(W_{\text{raw}} + W_{\text{raw}}^\top)\right). \quad (16)$$

Proposition 2 (Well-posedness). *For $\Lambda_k > 0$ (via softplus) and $w_{ij} > 0$ (via softplus on bilinear form), $A_k = L_W + \text{diag}(\Lambda_k)$ is symmetric positive definite, guaranteeing a unique solution.*

The system is solved via CG [Hestenes & Stiefel, 1952] with 40–60 iterations. A custom `torch.autograd.Function` implements implicit differentiation via the adjoint method, requiring only $O(N)$ memory. An optimized Rust kernel [Matsakis & Klock, 2014] with Rayon parallelism provides $\sim 7\times$ speedup.

3.2 Recurrent Multigrid Architecture

The full architecture (Figure 3) repeats a two-level multigrid V-cycle for R rounds:

Cell encoder. $\mathbf{h}_i = \text{MLP}(\mathbf{x}_i \| \hat{\mathbf{y}}_i^{(r-1)} \| \mathbf{p}_i \| r / (R-1))$ produces per-cell features incorporating input, previous predictions, position, and round fraction.

Damping and source. Both are produced by 3-layer MLPs reading a rich feature vector: \mathbf{h} , position, previous ψ , 8-way directional scans, cross-field statistics, and unpooled object features from the previous round’s V-cycle.

Directional scans. Cumulative sums of normalized ψ along 8 directions (4 cardinal + 4 diagonal) provide each cell with aggregated row, column, and diagonal information without explicit long-range edges.

Object layer (multigrid V-cycle). Cells are softly assigned to K_{obj} learned clusters via $A = \text{softmax}(\text{MLP}(\tilde{\psi} \| \mathbf{p}) / \tau)$. Cell features are pooled ($A^\top \cdot \mathbf{f}$), a coarse Poisson equation is solved on the object graph, and results are prolonged back ($A \cdot \mathbf{o}^{\text{out}}$). This implements a classical two-level V-cycle [Briggs et al., 2000] with *learned* restriction and prolongation operators.

Decoder. An MLP maps the full feature set (fields, dissipation, cell features, position, scans, unpooled objects) to task-specific outputs.

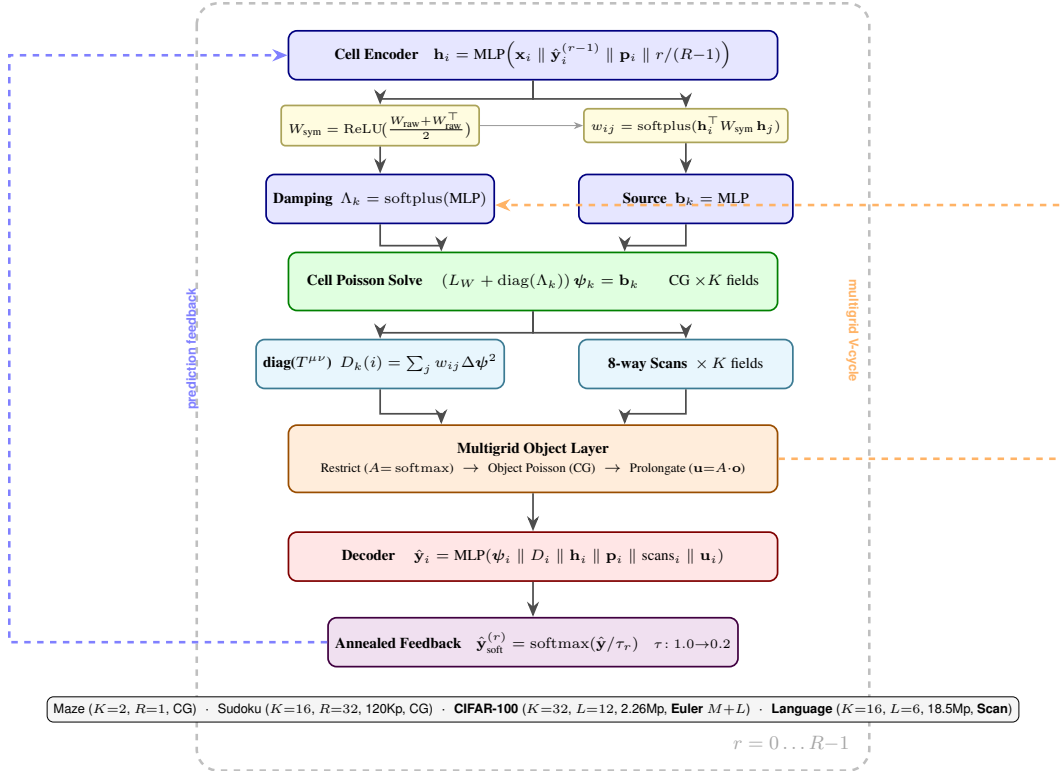


Figure 3: **Metriplector architecture.** A single round of the recurrent V-cycle (repeated R times with shared weights). The cell encoder produces per-cell features \mathbf{h} from input, previous predictions, and round fraction. Learned symmetric conductances w_{ij} define the graph Laplacian. Damping and source MLPs produce per-cell screening and forcing terms. K independent screened Poisson equations are solved via CG. The dissipation readout $D_k = \sum_j w_{ij} (\psi_i - \psi_j)^2 \approx |\nabla \psi_k|^2$ extracts the diagonal of the stress-energy tensor (the same $T^{\mu\nu}$ readout used in CIFAR-100, cf. Section 5); 8-way directional scans add global context. The multigrid object layer restricts to learned soft-assignment groups, solves a coarse Poisson, and prolongates back. The decoder reads all features to produce per-cell predictions, fed back via annealed softmax ($\tau: 1.0 \rightarrow 0.2$). **Blue:** prediction feedback across rounds. **Orange:** multigrid V-cycle within each round. Reasoning domains (maze, Sudoku) share this CG-based architecture with different K , R , and output dimension C ; CIFAR-100 uses a distinct Euler-based instantiation (Section 3.5).

Prediction feedback. Softmax predictions are fed back with linearly annealing temperature: $\tau_r = 1.0 \cdot (1 - r/(R-1)) + 0.2 \cdot r/(R-1)$. Early rounds explore; late rounds commit—analogueous to simulated annealing [Kirkpatrick et al., 1983].

3.3 Domain-Specific Adaptations

Table 2: **Domain configurations.** All variants share the metriplectic formalism; domains differ in which GENERIC channels are active, the solver, and domain-specific adaptations. Sudoku and CIFAR-100 implement the same underlying physics (Section 5): both read $T^{\mu\nu}$ from evolved fields.

Domain	Graph	K	Depth	K_{obj}	Output	Params	Dynamics
Maze	4-conn grid	2	$R=1$	—	5 classes	43.8K	CG, M only
Sudoku	8-conn lattice	16	$R=32$	16	9 digits	120K	CG, M only
CIFAR-100	2D grid 16×16	32	$L=12$	—	100 classes	2.26M	Euler , $M+L$
Language	Causal 1D chain	16	$L=6$	—	1024 tokens	18.5M	Scan , M causal

Maze. The simplest variant: a single Poisson solve ($R = 1$). Cell types are encoded as anonymous integer indices—the model never receives labels like “wall” or “corridor.” The conductance matrix $W \in \mathbb{R}^{4 \times 4}$ discovers wall/corridor structure from data alone. We introduce λ/N scaling—normalizing the damping term by the number of nodes—to keep the spectral balance of the graph Laplacian constant across grid sizes.

Sudoku. The richest variant: 32 recurrent multigrid rounds with $K = 16$ fields and $K_{\text{obj}} = 16$ objects. Digits are encoded as anonymous indices; the graph is a pure 8-connected spatial lattice with no row/column/box edges. All Sudoku structure must be discovered by the model from data alone (zero structural injection—no row, column, or box edges are provided; the model receives digit values but no encoding of the constraint rules). The feature readout $D_k(i) = \sum_j w_{ij}(\psi_k(i) - \psi_k(j))^2$ is the discrete analog of the gradient energy $|\nabla\psi_k|^2$ —equivalently, the diagonal of the stress-energy tensor $T_{kk}^{\mu\mu}$ that the CIFAR-100 variant computes via learned gradient convolutions (Section 5). The object layer’s soft assignment $\rho = \text{softmax}(\text{MLP}(\psi, \mathbf{p})/\tau)$ with coarse-graining $\psi^{(1)} = \rho^\top \psi^{(0)}$ performs learned spatial pooling analogous to block-spin coarse-graining. Difficulty-stratified sampling overweights hard puzzles during training.

3.4 Language Modeling: Causal Metriplectic Dynamics

For causal language modeling (Figure 4), the screened Poisson equation is instantiated on a *causal* 1D chain graph: each token position i receives information only from positions $j < i$. On this causal chain, the Poisson equation reduces to a first-order linear recurrence:

$$\psi_i = \alpha_i \cdot \psi_{i-1} + \beta_i, \quad \alpha_i = \frac{w_i}{w_i + \lambda_i}, \quad \beta_i = \frac{b_i}{w_i + \lambda_i}, \quad (17)$$

where w_i is a learned edge conductance and λ_i, b_i are per-position damping and source. This affine recurrence is solved exactly in $O(N \log N)$ via the Blelloch parallel associative scan [Blelloch, 1990], preserving strict autoregressive causality while providing efficient GPU-parallel execution.

Progressive multigrid. A three-level causal hierarchy provides multi-scale context: token-level scans (local syntax), chunk-level scans with shifted pooling (phrase/sentence), and section-level scans (paragraph/topic). Different layers receive different hierarchy levels—early layers see only local context, later layers access progressively coarser scales.

Cross-field interactions. Low-rank outer products $\psi \otimes \psi$ and $\psi \otimes D$ (where $D_i = w_i(\psi_i - \psi_{i-1})^2$ is the local dissipation) capture pairwise field correlations, providing the inter-field coupling that attention achieves via multi-head dot products.

Stacked non-shared layers. As with CIFAR-100, each of the $L=6$ layers has independent weights for source/damping MLPs, edge conductances, and the round MLP that integrates ψ features into the hidden state \mathbf{h} —a design principle shared across all deep Metriplector instantiations.

3.5 CIFAR-100: Full Metriplectic Layers

Image classification requires a fundamentally different instantiation of the metriplectic formalism (Figure 5). Rather than solving for equilibrium (maze, Sudoku), the CIFAR-100 architecture evolves K physics fields ψ through 12 *non-shared* layers of Euler integration, with a separate representation $\mathbf{h} \in \mathbb{R}^D$ ($D=128$) carrying class information via residual connections.

The operator-from-input principle. The representation \mathbf{h} defines the physics that ψ evolves under—there is no circular dependence. Five $\text{Conv}1 \times 1$ projections derive operator coefficients from \mathbf{h} :

$$\begin{aligned} \psi &= W_\psi \mathbf{h}, & \sigma &= \text{softplus}(W_\sigma \mathbf{h}), \\ \alpha &= W_\alpha \mathbf{h}, & \gamma &= \text{softplus}(W_\gamma \mathbf{h}) + 0.1, \\ \mathbf{s} &= \text{clamp}(W_s \mathbf{h}, \pm 5), \end{aligned} \quad (18)$$

where each W is a learned $K \times D$ matrix. The field ψ is created fresh from \mathbf{h} in every layer. Ablations confirm this design: recurrent ψ degrades accuracy by 3.4 points, and letting ψ build its own operator costs 14.3 points (Table 4).

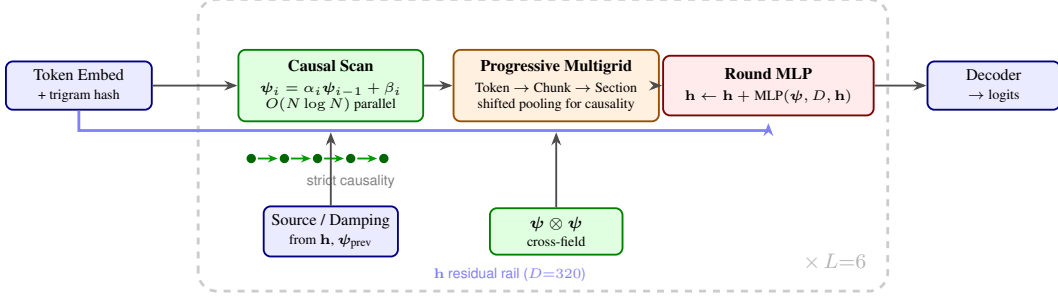


Figure 4: **Causal Poisson language model.** Tokens are embedded and passed through $L=6$ non-shared CausalPoissonLayers. Each layer solves the causal Poisson recurrence via $O(N \log N)$ parallel associative scan, applies progressive multigrid (token \rightarrow chunk \rightarrow section scales with shifted pooling for causal safety), computes cross-field outer products $(\psi \otimes \psi)$, and integrates all features into the hidden state \mathbf{h} via a round MLP with residual connection.

The K -field bottleneck. The representation $\mathbf{h} \in \mathbb{R}^D$ ($D=128$) carries class information via residual connections; the physics fields $\psi \in \mathbb{R}^K$ ($K=32$) are where metriplectic dynamics operate. This mirrors multi-head attention: project to a small space, compute complete interactions ($K^2 = 1,024$ stress-energy features), and project back. The $\text{Conv}1 \times 1$ projection back to D selects which physics features matter for classification.

Readout via Noether’s theorem. After metriplectic evolution, the model must extract features from the evolved fields ψ and project them back into the representation \mathbf{h} . Rather than treating this as an arbitrary feature-engineering step, we derive the readout from *Noether’s theorem*: every continuous symmetry of the dynamics yields a conserved current, and these conserved currents are the natural observables of the field theory.

Spatial translation symmetry yields the *stress-energy tensor*:

$$T_{ab}^{ij} = \partial_i \psi_a \cdot \partial_j \psi_b, \quad (19)$$

where a, b index fields and i, j index spatial directions. We decompose this into physically meaningful components:

- **Energy density** (symmetric trace): $E_{ab} = \nabla \psi_a \cdot \nabla \psi_b$. For $a=b$: edge strength of field a (gradient magnitude). For $a \neq b$: whether fields a and b have co-located edges—a structural correlation measure.
- **Vorticity** (antisymmetric shear): $V_{ab} = \partial_x \psi_a \cdot \partial_y \psi_b - \partial_x \psi_b \cdot \partial_y \psi_a$. Non-zero at corners and junctions, where the gradient of one field is perpendicular to another’s. Zero along straight edges. Detects structural complexity.

The directional gradients $\partial_x \psi$, $\partial_y \psi$ are computed by learned depthwise convolutions (initialized as Sobel-like filters). The total feature count is K^2 : K diagonal energy terms + $K(K-1)/2$ cross-field energy terms + $K(K-1)/2$ vorticity terms.

We also evaluate two alternative readouts:

- **Field-curvature products**: $\psi_a \cdot \Delta \psi_b$ (symmetric, field value \times Laplacian) and $\psi_a \Delta \psi_b - \psi_b \Delta \psi_a$ (antisymmetric, cross-field twist), yielding $K + K(K-1)/2$ features. These mix field *values* with *second* derivatives—related to the stress tensor through integration by parts but not identical. The stress tensor uses *first* derivative products, which are sign-consistent (always non-negative for $a=b$) and geometrically cleaner.
- **Noether currents** (full symmetry set): momentum density $\psi \cdot \nabla \psi$ (translation), angular momentum $\mathbf{x} \times \mathbf{p}$ (rotation), dilation current $\mathbf{x} \cdot \mathbf{p}$ (scale), plus stress-energy. These incorporate spatial coordinates (\mathbf{x}, \mathbf{y}) , providing position-aware features—a physics-native positional encoding. Yields $5K + 3K(K-1)/2$ features.

The stress-energy readout achieves the best accuracy (Table 3), confirming that the conserved quantities of the spatial symmetry group are the most informative observables of the evolved field.

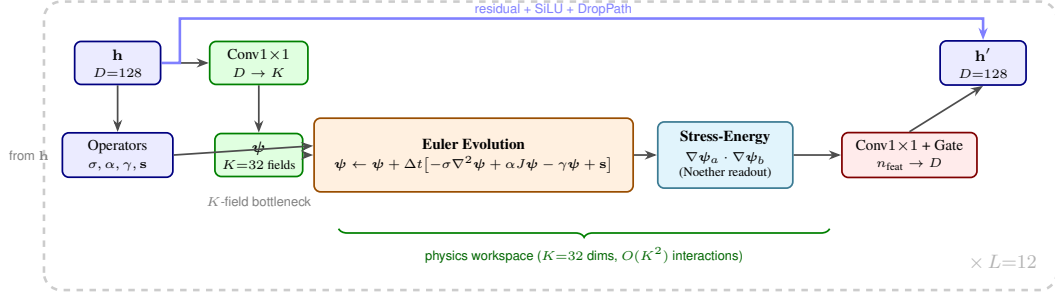


Figure 5: **CIFAR-100 metriplectic layer** ($\times 12$, non-shared weights). The representation \mathbf{h} ($D=128$) flows along the top via residual connections. Each layer projects \mathbf{h} down to $K=32$ physics fields ψ , evolves them under the full metriplectic equation (diffusion + advection + damping + source), extracts physically meaningful features via the stress-energy tensor (Noether readout), and projects back to D via gated mixing. The K -field bottleneck reduces pairwise interaction cost by $16\times$ compared to operating in the full D space.

A Conv1 \times 1 projection ($n_{\text{feat}} \rightarrow D$) with BatchNorm [Ioffe & Szegedy, 2015] and learned gating mixes the physics features back into \mathbf{h} via a residual connection with SiLU activation [Elfving et al., 2018] and stochastic depth [Huang et al., 2016].

4 Experiments

4.1 CIFAR-100 Image Classification

CIFAR-100 provides the strongest test of Metriplector’s scalability: 100 fine-grained classes at 32×32 resolution demand both spatial feature extraction and rich cross-class discrimination. This is the first domain where the full metriplectic structure (Section 2.4) is essential—the Poisson bracket J mediates the cross-field mixing needed to distinguish 100 classes.

Table 3: **CIFAR-100 results.** All Metriplector models: 12 layers, patch size 2, identical recipe (Adam [Kingma & Ba, 2015], lr= 3×10^{-3} , cosine, AutoAugment [Cubuk et al., 2019], label smoothing 0.1, 200 epochs).

Model	Params	Acc	Note
<i>Metriplector (ours, full $M+L$)</i>			
StressEnergy $K=32$ $s=8$	2.26M	81.03	Stress-energy, 8 sub
StressEnergy $K=32$ $s=3$	2.26M	80.6	3 substeps
StressEnergy $K=32$ $s=1$	2.26M	80.4	1 substep
Noether $K=32$	1.70M	79.8	Position readout
PhysicsSelects-V2 $K=32$	1.49M	78.4	Curvature readout
<i>Geometric algebra (CliffordNet [Ji, 2026])</i>			
CliffordNet-64 ($K=5$, inner)	8.6M	82.46	Full GA, no FFN
CliffordNet-32 ($K=3$, full)	4.8M	81.42	Full GA, no FFN
CliffordNet-Lite ($K=5$, diff)	2.6M	79.05	No FFN
CliffordNet-Nano ($K=2$, diff)	1.4M	77.82	No FFN
<i>Conventional architectures</i>			
DenseNet-BC [Huang et al., 2017]	25.6M	82.8	
ConvNeXt-T [Liu et al., 2022]	28.6M	82.0	
WRN-28-10 [Zagoruyko & Komodakis, 2016]	36.5M	81.1	
ResNet-110 [He et al., 2016]	1.7M	74.1	

Parameter efficiency. Metriplector achieves 81.03% with only 2.26M parameters—closing to within 1.8 points of DenseNet-BC (82.8%, 25.6M) while using **10–15 \times fewer parameters**. Among physics-inspired architectures, the closest comparison is CliffordNet [Ji, 2026], which grounds its dynamics in geometric algebra (Clifford product). At comparable parameter budgets, Metriplector

outperforms CliffordNet-Lite (79.05%, 2.6M) by +2.0 points with fewer parameters, and matches CliffordNet-32 (81.42%, 4.8M) at less than half the parameters. On a params-per-accuracy-point basis: WideResNet-28-10 uses 450K params/point, ConvNeXt-Tiny uses 349K, DenseNet-BC uses 309K, while our StressEnergy model uses only 28K—an order of magnitude more efficient. This efficiency gap reflects the inductive bias provided by the metriplectic structure. Multiple Euler substeps further improve accuracy (80.4% \rightarrow 80.6% \rightarrow 81.03% for $s=1, 3, 8$), confirming that deeper metriplectic evolution within each layer provides richer spatial information propagation. This efficiency stems from the K -field bottleneck: pairwise interactions occur in a $K=32$ dimensional physics space ($K^2 = 1,024$ stress-energy features from the $T^{\mu\nu}$ readout) rather than the full $D=128$ representation space (Figure 6).

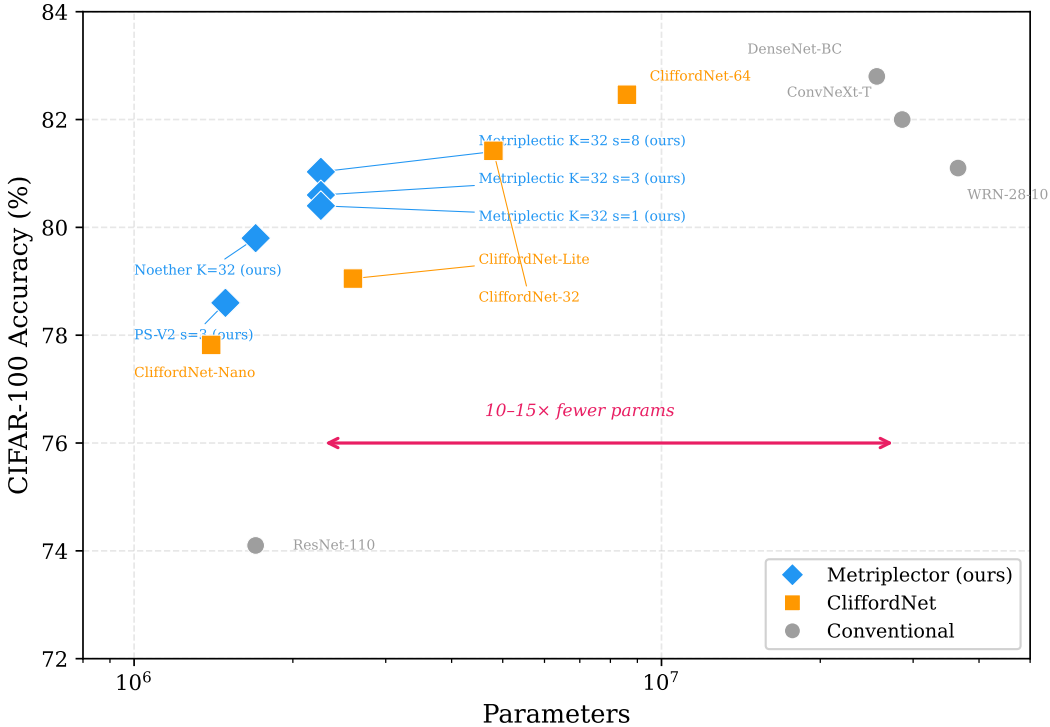


Figure 6: **CIFAR-100: Accuracy vs. parameters.** Metriplector variants (blue) achieve 80%+ accuracy with 2.26M parameters—10–15 \times fewer than conventional architectures (gray) at similar accuracy levels.

Table 4: **CIFAR-100 ablations.** *Top:* cumulative improvements from V1 (77.6%); each row adds one component on top of all previous rows; Δ is relative to V1. *Bottom:* component removal from V2 baseline (78.4%); Δ is the accuracy drop when that component is removed.

Ablation	Acc (%)	Δ from base
<i>Cumulative improvements (from V1 = 77.6%)</i>		
+ SiLU + BN residual engineering (V1 \rightarrow V2)	78.4	+0.8
+ 3 Euler substeps (more propagation per layer)	78.6	+1.0
+ Noether currents (p_x, p_y, L, D , position-aware)	79.8	+2.2
+ Stress-energy + 8 substeps ($\nabla\psi \times \nabla\psi$, K^2 features)	81.03	+3.4
<i>Component removal (from V2 baseline = 78.4%)</i>		
– $K=32$ fields ($\rightarrow K=16$)	74.5	–3.9
– Fresh ψ per layer (\rightarrow recurrent ψ)	75.0	–3.4
– Operator from \mathbf{h} (\rightarrow operator from ψ)	64.1	–14.3
– Poisson bracket J (\rightarrow diffusion only)	65.0	–13.4

The ablations confirm that both branches of the metriplectic formalism are essential: removing the Poisson bracket J (the antisymmetric cross-field coupling that mediates advection) costs **13.4 points**. The stress-energy tensor readout—derived from Noether’s theorem connecting spatial symmetries to conserved quantities—provides the most effective feature extraction (Figure 7).

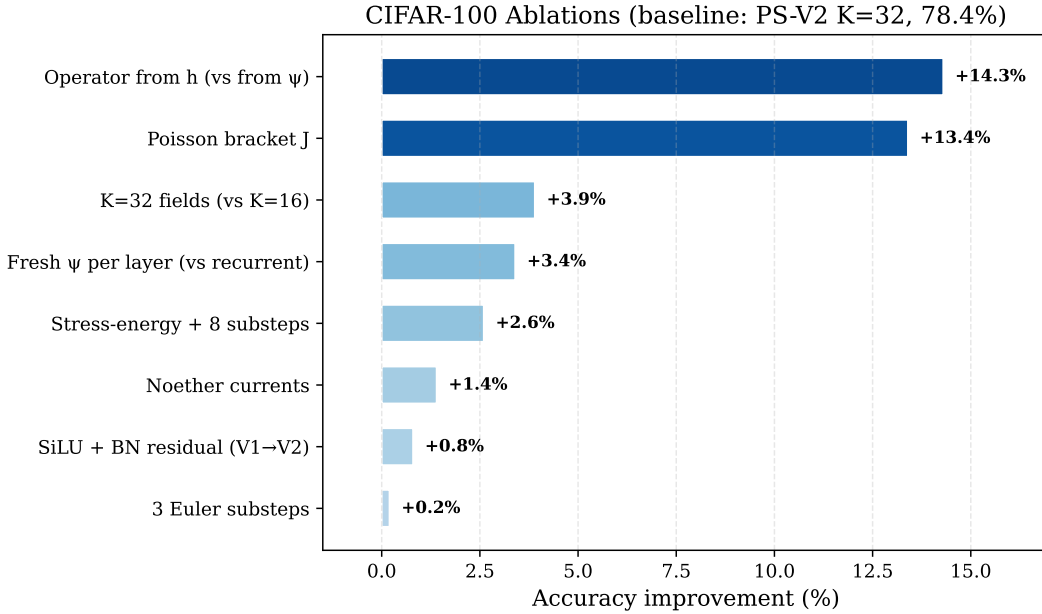


Figure 7: **CIFAR-100 ablation impacts.** Accuracy improvement from each architectural component relative to the PhysicsSelects-V2 $K=32$ baseline (78.4%). The operator-from- h principle (+14.3%) and the Poisson bracket J (+13.4%) are the most important factors. Fresh ψ per layer (+3.4%) validates the non-recurrent physics design.

Physics diagnostics. Figure 8 reveals the learned Poisson tensor J across layers: singular values appear in degenerate pairs (a structural signature of skew-symmetry), and the effective rank grows with depth while the null-space dimensions reflect the intrinsic rank deficiency of skew-symmetric matrices. The J Frobenius norm grows from 3.8 (L0) to 10.9 (L11), suggesting deeper layers develop stronger cross-field coupling. The ψ field magnitude and spatial variance across layers show a sharp increase at L11, reflecting the final layer concentrating discriminative features before the stress-energy readout.

Field specialization and dynamics budget. Figure 9 reveals how the 32 ψ fields specialize across layers. Field magnitudes remain moderate (0.2–0.5) through L0–L10, with a dramatic spike at L11 where several fields exceed magnitude 1.0—the model concentrates discriminative features into specific field channels before the stress-energy readout. Spatial variance follows the same pattern: most fields maintain low variance (spatially uniform activations) in early layers, developing strong spatial structure only at L11 where the network must localize class-specific features. This pattern—stable evolution followed by a concentrated burst—is consistent with the metriplectic dynamics operating as a controlled energy cascade.

Figure 10 shows the representation dynamics budget across layers: the hidden state h grows monotonically from $|h| = 0.017$ (L0) to 0.126 (L11), with each layer contributing a controlled update Δh that grows proportionally. The learned step size γ increases with depth (0.12 \rightarrow 0.22), allowing later layers to make larger representational changes—the architecture self-organizes an expanding dynamics budget.

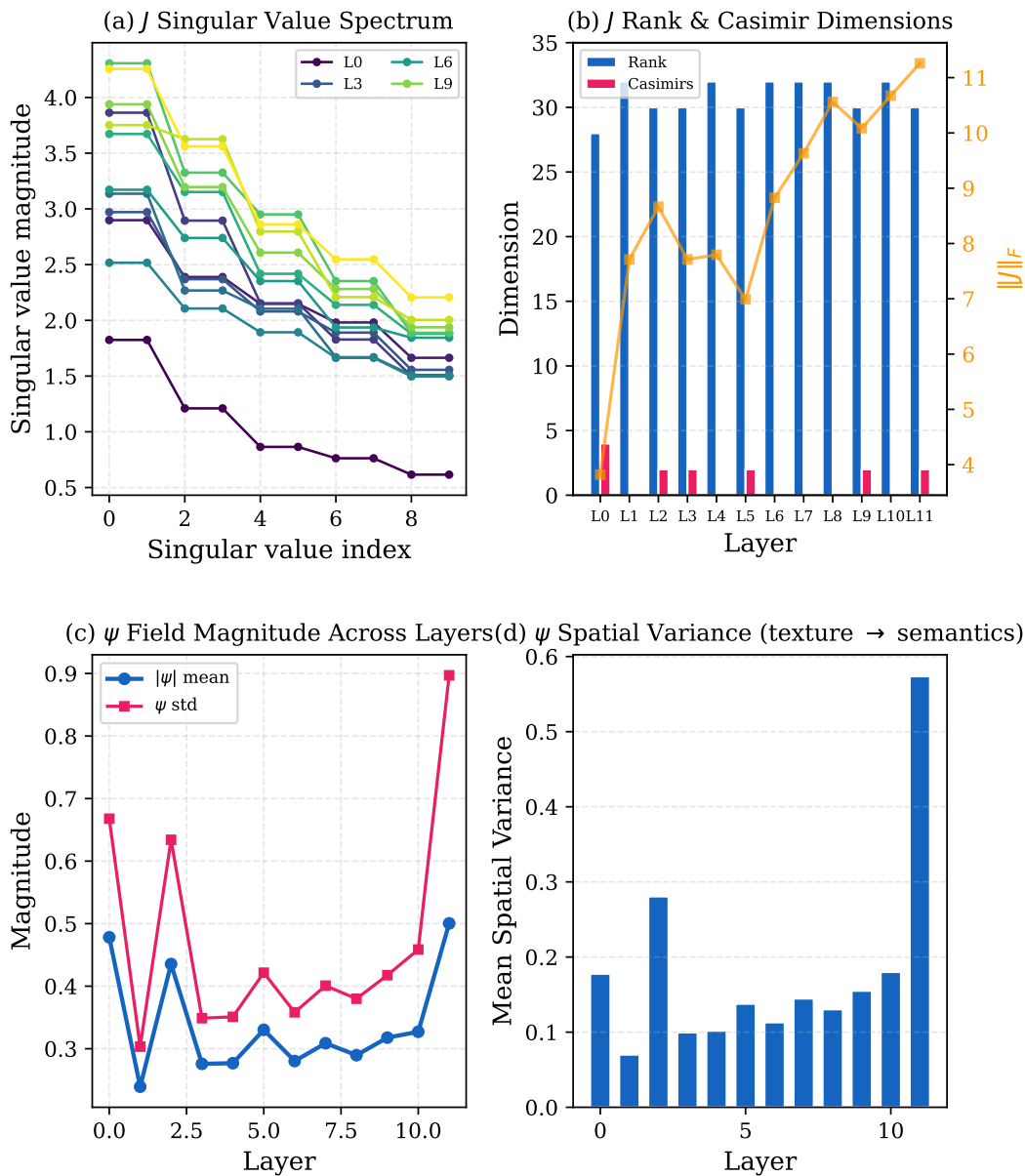


Figure 8: **CIFAR-100 physics diagnostics across 12 layers.** (a) Singular value spectrum of the learned Poisson tensor J —values appear in degenerate pairs, the hallmark of skew-symmetric structure. (b) J effective rank and null-space dimensions; $\|J\|_F$ grows monotonically with depth, indicating stronger cross-field coupling in later layers. (c) ψ magnitude and standard deviation remain stable (0.25–0.5) across L0–L10, with a sharp spike at L11 before the stress-energy readout. (d) Spatial variance increases at the final layer, reflecting transition from distributed texture to localized semantic features.

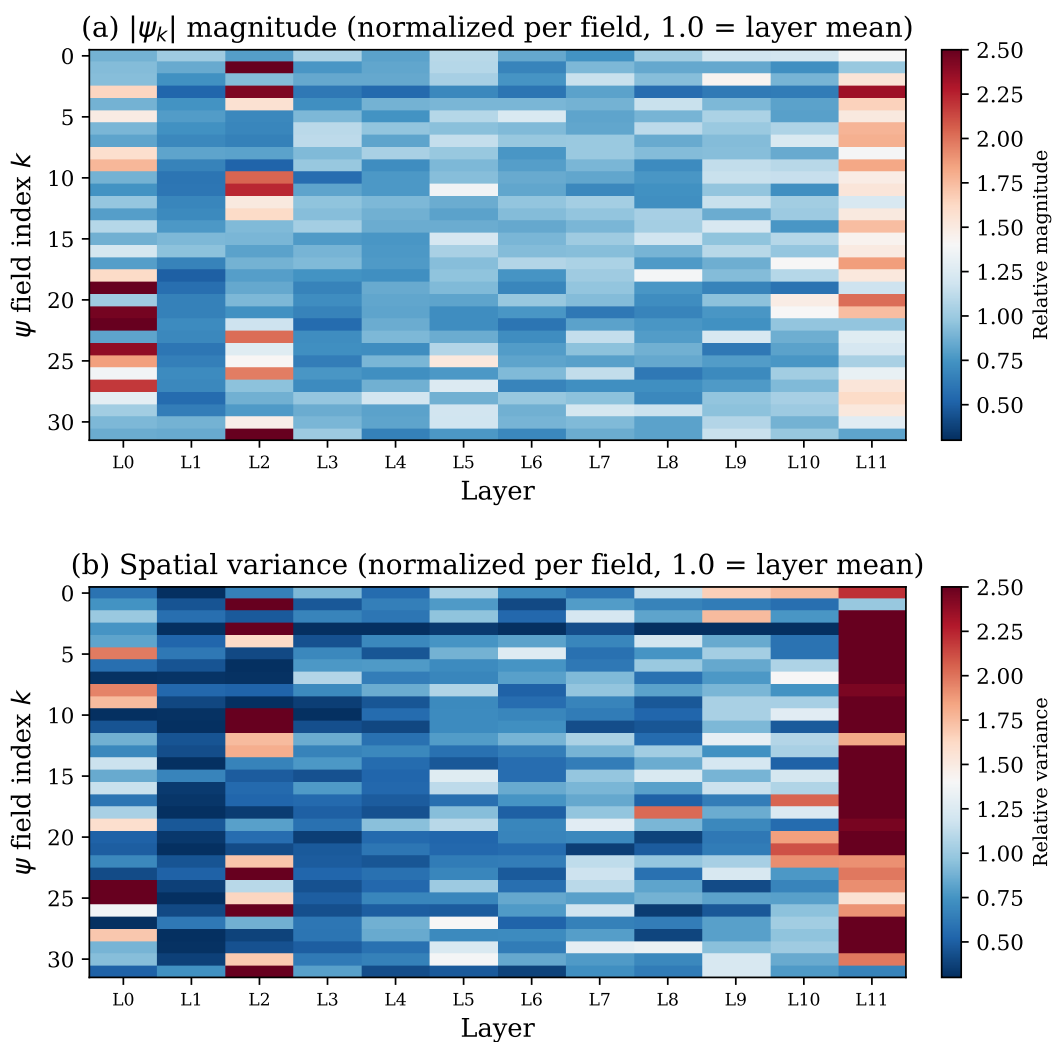


Figure 9: ψ field specialization across 12 layers (32 fields \times 12 layers). (a) Field magnitude: most fields remain moderate through L0–L10, with a sharp spike at L11 where specific fields (e.g., $k=3, 20, 21$) concentrate discriminative features. (b) Spatial variance: early layers develop spatially uniform fields (low variance); L11 shows dramatic spatial structure as the model localizes class-specific features before readout.

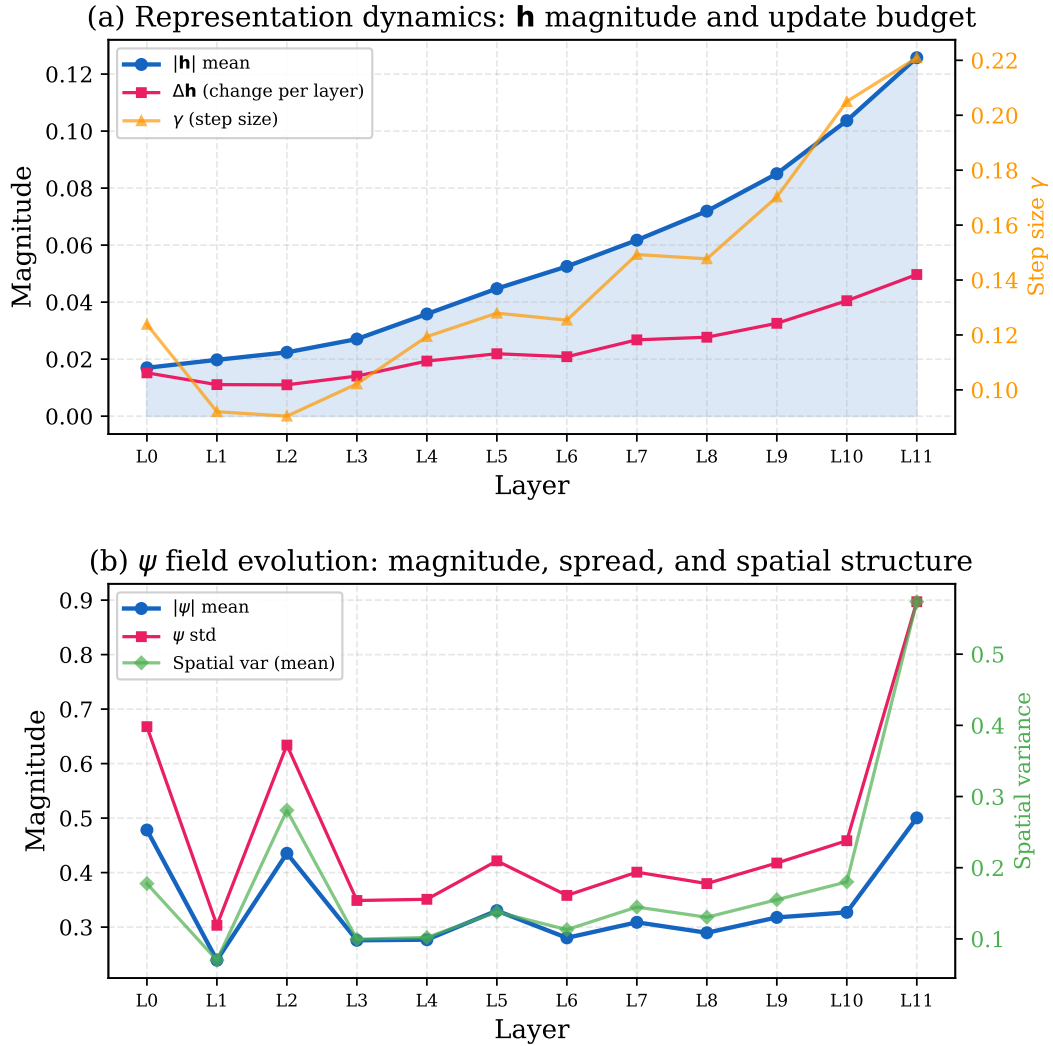


Figure 10: **CIFAR-100 forward dynamics budget.** (a) Hidden state \mathbf{h} : magnitude and per-layer update $\Delta \mathbf{h}$ both grow monotonically; the step size γ increases from 0.12 to 0.22, self-organizing an expanding dynamics budget. (b) ψ fields: magnitude and standard deviation are stable (0.25–0.5) across L0–L10, with spatial variance spiking at L11.

4.2 Sudoku Constraint Satisfaction

Metriplector achieves **99.4%** cell accuracy and **97.2%** exact solve rate on 9×9 Sudoku with *zero structural injection*: the graph has only 8-connected spatial edges (544 total), and no row, column, or box structure is provided (120K parameters, 10K training puzzles, $R=32$ rounds). Per difficulty: easy 99.8%, medium 99.6%, hard 99.0%. The multigrid object layer is the largest single contributor (+10% cell accuracy); increasing rounds from 16 to 32 adds +4.8%; scaling from 500 to 10K training puzzles adds +6.4%. Data augmentation (digit permutation, spatial rotations) consistently hurts.

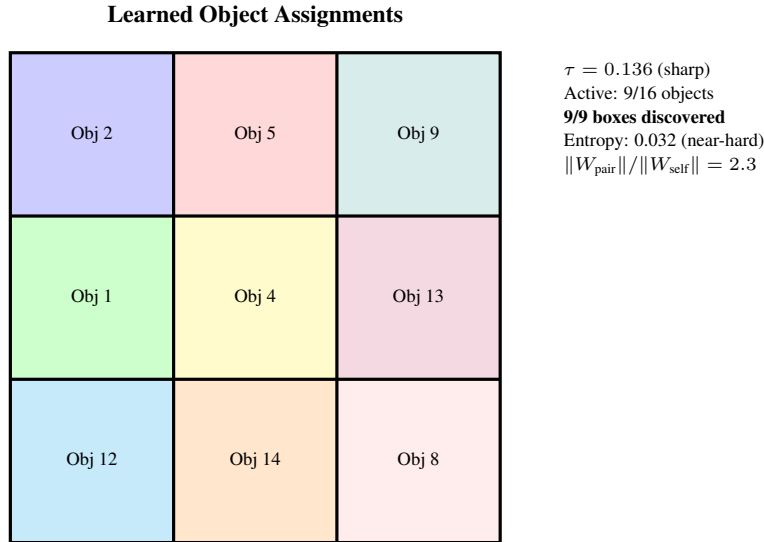


Figure 11: **Emergent box discovery in Sudoku.** The object layer discovers all 9 Sudoku 3×3 boxes from an 8-connected spatial lattice with no box-level supervision. Assignments are sharp ($\tau=0.136$, entropy ≈ 0.032) and static across all puzzles.

Emergent box discovery. Post-hoc analysis reveals that the object layer discovers **all 9** Sudoku 3×3 boxes from the 8-connected spatial lattice (Figure 11). Assignment temperature $\tau=0.136$ produces near-deterministic groupings (mean entropy 0.032), with exactly 9 of 16 available objects active—each containing exactly 9 cells aligned to box boundaries. The cross-object interaction ratio $\|W_{\text{pair}}\|/\|W_{\text{self}}\| = 2.3$ indicates the model prioritizes inter-box communication. Directional scans handle row/column constraints while objects handle box constraints—this division of labor emerges from training without any structural hints.

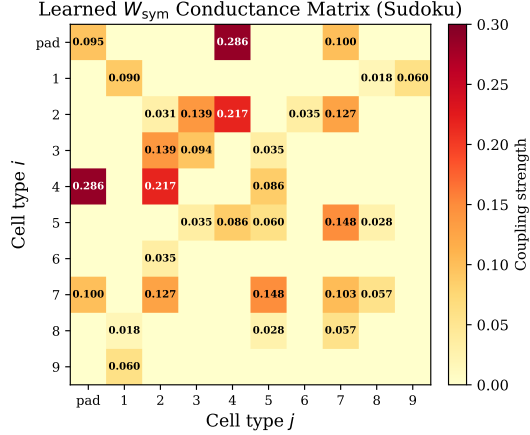


Figure 12: **Learned conductance matrix** W_{sym} (Sudoku). Entries show coupling strength between cell types (digits 1–9 and padding). The model learns sparse, structured couplings: strong links ($4 \leftrightarrow \text{pad}$, $2 \leftrightarrow 4$, $5 \leftrightarrow 7$) emerge without supervision.

4.3 Language Modeling

Language modeling tests whether the metriplectic formalism can compete with transformers on their home turf: autoregressive next-token prediction on the FineWeb dataset [Penedo et al., 2024] with a 1024-token SentencePiece vocabulary, measuring bits per byte (BPB, lower is better). All models respect the ≤ 16 MB artifact size constraint of the Parameter Golf challenge.

Table 5: **Language modeling results.** BPB on FineWeb validation. All models ≤ 16 MB.

Model	Params	BPB ↓	Tokens	Note
Metriplector (Stacked v6)	18.5M	1.182	2.0B	1×GH200, 2.6 hr
GPT baseline	9.8M	1.224	7.2B	8×H100, 10 min
PG leaderboard SOTA	—	1.119	—	+TTT, EMA, etc.

The Stacked v6 model uses 6 non-shared CausalPoissonLayers with progressive multigrid and cross-field outer products ($\psi \otimes \psi$), trained for 30K steps on 512-token sequences. It achieves **1.182 BPB**, compared to the GPT baseline (1.224 BPB, post-quantization)—a difference of 0.042 BPB while seeing **3.6× fewer training tokens** (2.0B vs. 7.2B). The comparison is not compute-matched: GPT trains on 8 GPUs in 10 minutes (80 GPU-minutes) while our model uses a single GPU for 2.6 hours (156 GPU-minutes, $\sim 2\times$ more). Our model uses 512-token sequences vs. GPT’s 1024; BPB is normalized per byte, but longer-context modeling is inherently harder. The PG leaderboard SOTA (1.119 BPB) exceeds both models using techniques orthogonal to architecture.

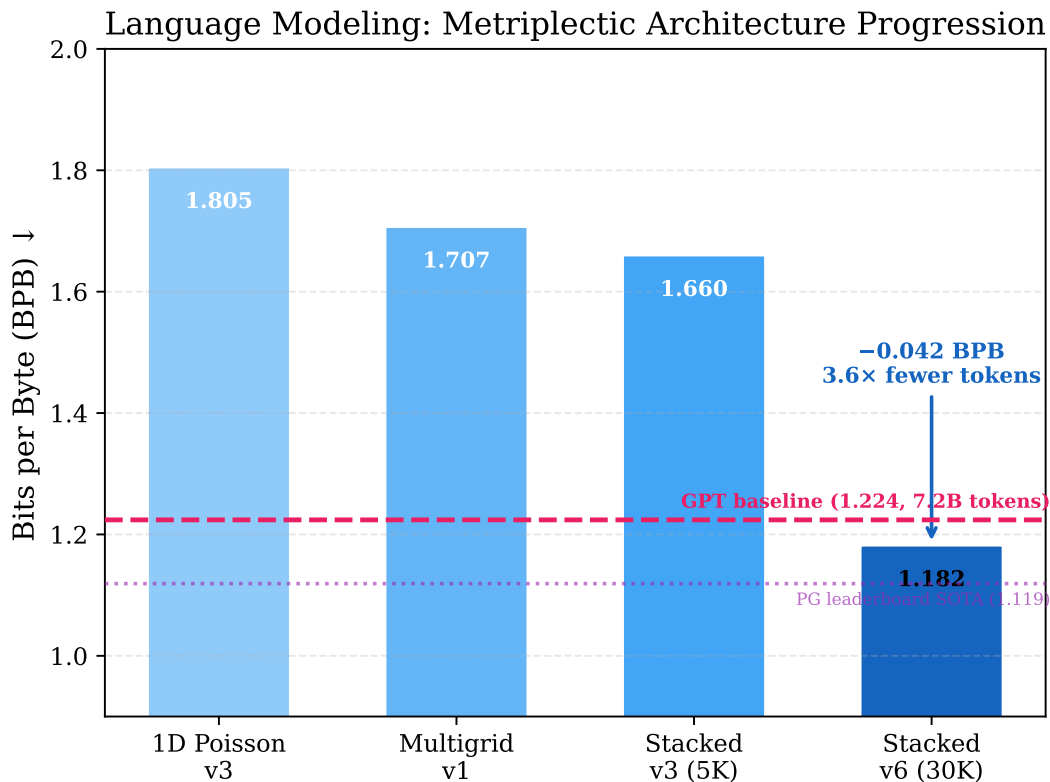


Figure 13: **Language modeling BPB progression.** GPT baseline (1.224 BPB, dashed) shown for reference; Metriplector reaches 1.182 BPB with 3.6× fewer training tokens.

4.4 Maze Pathfinding

Table 6: **Maze results.** F1 score on tree-maze path prediction. Metriplector achieves F1 = 1.0 on 15×15 and F1 = 0.95–0.99 on 39×39 across seeds.

Model	Params	F1 (15×15)	F1 (39×39)	Steps
Harmonic baseline	0	0.47	—	—
MetriNet Phase 7.3B	9,100	0.59	—	4,000
Metriplector 7.53K ($K=2$)	43.8K	1.00	0.43	10,000
Metriplector 7.530 (λ/N)	43.8K	1.00	0.95–0.99	10,000

The maze domain demonstrates Metriplector’s most striking result: **robust size generalization**. Training on 250 mazes of size 15×15 and evaluating on 200 mazes of size 39×39 (6.8× more cells, 17× longer paths), the model achieves F1 = 1.0 on 15×15 and F1 = 0.95–0.99 on 39×39 across seeds (43.8K parameters). Our λ/N scaling preserves the spectral balance of the graph Laplacian across grid sizes.

Emergent type discovery. The learned conductance matrix $W \in \mathbb{R}^{4 \times 4}$ discovers that one cell type (walls) should have near-zero conductance while another (corridors) should conduct freely. The source encoder learns to inject positive charge at the source and negative at the goal. All of this emerges from the anonymous type principle—the model receives only integer indices, never semantic labels.

Table 7: **Cross-domain results.** One metriplectic formalism, four instantiations.

Domain	Params	Result	Key Finding
Maze 15→39	43.8K	F1=0.95–0.99	Robust size transfer
Sudoku 9×9	120K	97.2% exact	9/9 box discovery, zero injection
CIFAR-100	2.26M	81.03% acc	10–15× fewer params vs. DenseNet
Language	18.5M	1.182 BPB	3.6× fewer tokens vs. GPT

4.5 Cross-Domain Summary

A single metriplectic formalism, instantiated differently per domain, achieves competitive results across all four tasks with consistently fewer parameters and training samples than conventional approaches (Table 7).

5 Discussion

Physics and learning are complementary. Metriplector is not purely physics-based. The Poisson fields provide *spatial propagation*; the MLPs (cell encoder, damping, source, decoder) perform *learned reasoning*. Neither alone suffices: pure Poisson reaches ~68% on Sudoku; adding learned components reaches 99.4% cell accuracy. The physics provides the right inductive bias—global equilibrium, conservation laws, structured readout—while the learned components adapt this bias to specific tasks.

The stress-energy tensor as readout. The most important architectural finding is that the stress-energy tensor $T^{\mu\nu}$ —the conserved quantity associated with spatial translation symmetry—provides the most effective readout from evolved fields. The gradient correlation $\nabla\psi_a \cdot \nabla\psi_b$ is the same computation as the structure tensor, which has been effective for edge and corner detection in classical computer vision since the 1980s [Harris & Stephens, 1988, Förstner, 1986]. Applied to learned fields evolved via metriplectic dynamics rather than raw image gradients, it arises from Noether’s theorem as the conserved quantity of spatial translation symmetry—and generalizes far beyond vision: the same readout principle provides effective feature extraction for image classification, constraint satisfaction, and language modeling across all domains tested. On CIFAR-100, the full $T^{\mu\nu}$ decomposition (gradient energy $E_{ab} = \nabla\psi_a \cdot \nabla\psi_b$ plus vorticity $V_{ab} = \nabla\psi_a \times \nabla\psi_b$) outperforms both field-curvature products (+2.6 points) and Noether current readouts (+1.2 points) in controlled ablations (Table 4).

This readout unifies two domains that appear superficially different. In Sudoku, the “dissipation” feature

$$D_k(i) = \sum_j w_{ij} (\psi_k(i) - \psi_k(j))^2 \quad (20)$$

is the discrete approximation to $|\nabla\psi_k|^2$ —exactly the diagonal of $T_{kk}^{xx} + T_{kk}^{yy}$ that CIFAR-100 computes via learned gradient convolutions. The CIFAR variant additionally extracts the full off-diagonal terms; extending the Sudoku readout to the full $T^{\mu\nu}$ is a natural next step. That the same physics-derived observable emerges as optimal in both recognition and constraint satisfaction supports the claim that $T^{\mu\nu}$ is a natural feature space for field-theoretic computation.

The operator-from-input principle. The most consequential design decision is that \mathbf{h} defines the operator and ψ is the solution—the representation configures the energy landscape, and the fields evolve on it. This principle, first discovered in the maze solver (where conductances are derived from cell type embeddings), transfers directly to all four domains. Violating it costs 14.3 accuracy points on CIFAR-100 (Table 4): when ψ builds its own operator, field collapse occurs (ψ magnitude <1% of \mathbf{h} by layer 12).

The metriplectic spectrum. Different tasks require different amounts of physical structure. Maze pathfinding and Sudoku constraint satisfaction are solved at *equilibrium*—the answer is the steady state of the dissipative branch (M only), computed exactly via conjugate gradient. Image recognition requires the full metriplectic structure: the antisymmetric Poisson bracket J provides the cross-field

mixing needed to distinguish 100 fine-grained categories (removing J costs 13.4 accuracy points). Language modeling uses a causal variant of the dissipative branch, solved via parallel scan. This spectrum—from pure dissipation to full metriplectic dynamics—provides a principled design space: the task determines which channels of the GENERIC equation to activate.

Zero structural injection. Across the spatial reasoning domains, Metriplector operates on minimal graph topologies: a 4-connected grid for mazes, an 8-connected spatial lattice for Sudoku. No task-specific structure is provided—no row, column, or box edges for Sudoku; no wall or corridor labels for mazes. The model discovers problem structure through the physics: the learned conductance matrix develops near-zero weights for walls and high weights for corridors; the multigrid object layer discovers all nine 3×3 Sudoku boxes from spatial adjacency alone (assignment temperature $\tau=0.136$, entropy ≈ 0.032 , 9 of 16 available objects active). This zero-injection principle is both a design choice and an empirical finding: it forces the physics to do the work, and the physics succeeds.

Limitations and future work. CIFAR-100 accuracy (81.03%) trails DenseNet-BC (82.8%, 25.6M) despite using $10 \times$ fewer parameters; scaling to ImageNet will test whether the K -field bottleneck remains sufficient. The causal Poisson language model is more sample-efficient ($3.6 \times$ fewer tokens) but less compute-efficient than GPT. The four domains use task-specific architectures built from the shared primitive; a single architecture that spans all four tasks remains an open goal. The multigrid object layer’s coarse-graining bears a structural resemblance to block-spin methods [Kadanoff, 1966]; whether this connection extends to the full renormalization group structure is an open question. The current Euler integrator for the full metriplectic dynamics (CIFAR-100) is first-order and does not preserve the symplectic structure of the Hamiltonian channel; replacing it with a leapfrog (Störmer-Verlet) integrator that reintroduces conjugate momentum would provide exact energy conservation along the Hamiltonian flow and may improve training stability at deeper evolution depths.

6 Related Work

Attention, transformers, and state space models. The attention mechanism [Bahdanau et al., 2015], generalized by the transformer [Vaswani et al., 2017], computes $\text{softmax}(QK^\top/\sqrt{d})V$ —a single-step weighted average on a complete graph that provides universal function approximation [Yun et al., 2020]. Vision Transformers [Dosovitskiy et al., 2021], Swin [Liu et al., 2021], and LLMs [Brown et al., 2020, Devlin et al., 2019, Touvron et al., 2023] demonstrate the effectiveness of this approach at scale. State space models—S4 [Gu et al., 2022], Mamba [Gu & Dao, 2024], and Mamba-2 [Dao & Gu, 2024]—reformulate sequence modeling as linear recurrences, achieving $O(N)$ complexity; Mamba-2 further showed that structured SSMs are equivalent to a form of structured attention. RWKV [Peng et al., 2023] takes a similar linear-recurrence approach. Our causal Poisson scan is also a linear recurrence ($O(N \log N)$ via parallel associative scan), but derives from the screened Poisson equation rather than signal processing or attention decomposition.

Energy-based models. Hopfield networks [Hopfield, 1982] showed that associative memory can be implemented as energy minimization. LeCun [LeCun, 2006] generalized this to Energy-Based Models (EBMs) for prediction. Boltzmann machines [Hinton & Sejnowski, 1984, Ackley et al., 1985] and their restricted variants [Smolensky, 1986] extended energy-based learning to generative modeling. Modern Hopfield networks [Ramsauer et al., 2021] connect energy-based retrieval to transformer attention. Equilibrium Propagation [Scellier & Bengio, 2017] bridges EBMs and backpropagation by computing gradients through equilibrium states—related to our CG-based equilibrium approach, though we solve the equilibrium exactly rather than approximating it. Metriplector uses both branches of the GENERIC equation, applying the coupled Hamiltonian-dissipative formulation to constraint satisfaction, image recognition, and language modeling.

Diffusion, flow, and score-based models. Diffusion models [Ho et al., 2020, Song et al., 2021] and their continuous-time formulation as score-based SDEs [Song et al., 2021] generate data by reversing a noise process governed by Langevin dynamics—a stochastic PDE where the learned score $\nabla_x \log p_t(x)$ plays a role analogous to a source term. Flow matching [Lipman et al., 2023] and rectified flows [Liu et al., 2023] simplify this to deterministic ODE transport, learning a ve-

locity field that maps noise to data. Poisson Flow Generative Models [Xu et al., 2022] use the Poisson equation specifically, connecting to our screened Poisson solver. These approaches share Metriplector’s premise that PDE dynamics can serve as the computational mechanism, but apply it to generation (sampling from learned distributions) rather than discriminative tasks (classification, constraint satisfaction, dynamics prediction). The key structural difference is that diffusion and flow models learn a *time-varying* vector field over data space, while Metriplector learns *spatial operators* (conductance, Poisson bracket, source) that define a fixed PDE whose solution provides the readout.

Hamiltonian and metriplectic learning. Neural ODEs [Chen et al., 2018] introduced continuous-depth networks via ODE solvers. Hamiltonian Neural Networks [Greydanus et al., 2019] learn energy functions whose symplectic dynamics model physical systems; Symplectic ODE-Net [Zhong et al., 2020] enforces structure via symplectic integrators. Lagrangian Neural Networks [Cranmer et al., 2020] use the Euler-Lagrange formulation. Hamiltonian Generative Networks [Toth et al., 2020] demonstrated that Hamiltonian structure can be leveraged for generative modeling from high-dimensional observations without restrictive domain assumptions. Port-Hamiltonian Neural Networks [Desai et al., 2021] and structure-preserving networks [Galimberti et al., 2023] guarantee non-vanishing gradients. The GENERIC framework [Grmela & Öttinger, 1997, Öttinger, 2005] provides a general framework for non-equilibrium dynamics via $\dot{z} = L\nabla E + M\nabla S$; Morrison [Morrison, 1998] established the Hamiltonian formulation for ideal fluids; Olver [Olver, 1993] connects Lie group symmetries to conservation laws. Metriplector instantiates the GENERIC equation on learned graphs, applying it to reasoning, recognition, and language.

Physics-inspired architecture primitives. CliffordNet [Ji, 2026] applies Clifford geometric products to neural features, computing symmetric (inner product) and antisymmetric (wedge product) interactions via an efficient sparse rolling mechanism. This decomposition is related to the symmetric-antisymmetric split underlying the metric and Poisson brackets in Metriplector, though CliffordNet derives from algebraic completeness of the geometric product while Metriplector derives from non-equilibrium thermodynamics. Kolmogorov-Arnold Networks (KAN) [Liu et al., 2024] replace fixed activation functions with learned univariate splines on graph edges, grounding architecture design in the Kolmogorov-Arnold representation theorem; Metriplector instead grounds its primitive in field-theoretic dynamics and Noether’s theorem. Geometric algebra foundations [Doran & Lasenby, 2003, Hestenes, 1984] provide the mathematical framework shared by several of these approaches. Group-equivariant CNNs [Cohen & Welling, 2016], E(2)-steerable networks [Weiler & Cesa, 2019], E(n) equivariant GNNs [Satorras et al., 2021], tensor field networks [Thomas et al., 2018], and SE(3)-equivariant models [Du et al., 2022] explore related symmetry-preserving architectures.

Equilibrium models. Deep Equilibrium Models [Bai et al., 2019] find fixed points of implicit layers. Monotone Operator Equilibrium Networks [Winston & Kolter, 2020] guarantee existence and uniqueness. Our Poisson solve is a single-step equilibrium computation with guaranteed convergence (SPD system matrix), avoiding the iterative fixed-point search that DEQs require.

Differentiable optimization layers. OptNet [Amos & Kolter, 2017] embeds quadratic programs in neural networks. Differentiable convex optimization layers [Agrawal et al., 2019] generalize this. Vlastelica et al. [Vlastelica et al., 2020] differentiate through blackbox combinatorial solvers. Our CG solver with adjoint implicit differentiation [Hestenes & Stiefel, 1952, Shewchuk, 1994] follows this tradition but exploits SPD structure for efficient $O(N)$ memory gradients.

Physics-informed and physics-simulation networks. PINNs [Raissi et al., 2019, Karniadakis et al., 2021] encode PDE residuals as soft constraints. Neural operators [Li et al., 2021] and DeepONet [Lu et al., 2021] learn mappings between function spaces. Graph Network Simulators [Sanchez-Gonzalez et al., 2020, Pfaff et al., 2021] and message-passing PDE solvers [Brandstetter et al., 2022] learn physics from data on meshes. In contrast to soft-constraint approaches, the Metriplector CG solver finds the exact PDE equilibrium, which guarantees physical consistency of the solution.

Graph neural networks and spectral methods. Message Passing Neural Networks [Gilmer et al., 2017, Scarselli et al., 2009, Battaglia et al., 2018] provide a general framework for learned computation on graphs; see Bronstein et al. [2021] and Wu et al. [2020] for surveys. Spectral approaches—ChebNet [Defferrard et al., 2016], spectral CNNs [Bruna et al., 2014]—operate on graph Laplacian

eigenvectors, connecting to spectral graph theory [Chung, 1997, Spielman, 2007]. GCN [Kipf & Welling, 2017], GAT [Veličković et al., 2018], and DeepGCNs [Li et al., 2019] learn spatial aggregation rules. Xu et al. [Xu et al., 2019] characterized GNN expressiveness via the Weisfeiler-Leman hierarchy. Topping et al. [Topping et al., 2022] showed that over-squashing in GNNs relates to graph curvature; Alon & Yahav [Alon & Yahav, 2021] identified the information bottleneck. The Poisson solve computes global equilibrium in a single pass; information propagation range is controlled by the damping parameter λ rather than by message-passing depth, which relates to the over-squashing phenomenon identified by Topping et al. [2022] and Alon & Yahav [2021].

Multigrid methods and learned pooling. Classical multigrid [Briggs et al., 2000, Trottenberg et al., 2001, Hackbusch, 1985] accelerates PDE solvers via fine-coarse cycling. He & Xu [He & Xu, 2019] showed that CNNs can be interpreted as multigrid iterations. U-Net [Ronneberger et al., 2015] implements a learned V-cycle. DiffPool [Ying et al., 2018] introduced learned soft-assignment graph pooling, where a GNN predicts cluster assignments and pools node features accordingly. Our object layer follows this restrict-solve-prolongate pattern, with the distinction that the coarse-level computation is a Poisson solve rather than further message passing.

Neural Sudoku and constraint satisfaction. Sudoku is NP-complete to solve in general [Yato & Seta, 2003], though the standard 9×9 case is tractable; Felgenhauer & Jarvis [Felgenhauer & Jarvis, 2006] enumerate valid grids. Recurrent Relational Networks [Palm et al., 2018] solve Sudoku via message passing on a constraint graph ($>96\%$ board accuracy). SATNet [Wang et al., 2019] embeds a differentiable MAXSAT solver; Zhang et al. [2021] explore neural logic machines. All inject constraint structure (row, column, box edges or MAXSAT solvers) into the architecture. Metriplector operates on a minimal 8-connected spatial grid without injecting constraint structure.

Neural algorithmic reasoning. Veličković & Blundell [Velivckovic & Blundell, 2021] formalize neural algorithmic reasoning; the CLRS benchmark [Veličković et al., 2022] evaluates neural networks on classical algorithms. GNN approaches [Ibarz et al., 2022, Tang et al., 2020] can learn algorithms but struggle with out-of-distribution sizes. On maze pathfinding, the λ/N scaling of the graph Laplacian enables generalization from 15×15 training grids to 39×39 evaluation grids (F1 = 0.95–0.99).

7 Conclusion

The stress-energy tensor $T^{\mu\nu}$, the conserved quantity of spatial translation symmetry, provides an effective and principled readout from learned field dynamics—this is the central finding of this work. Built on this observation, Metriplector instantiates the metriplectic framework as a neural architecture primitive across four domains: F1 = 1.0 on maze pathfinding (43.8K parameters) with robust size generalization; 97.2% exact Sudoku solve rate (120K parameters) with zero structural injection; 81.03% on CIFAR-100 (2.26M parameters); and 1.182 BPB on language modeling with $3.6 \times$ fewer training tokens than a GPT baseline.

Three design principles underpin these results and transfer across domains: (1) the *operator-from-input* separation, where the representation \mathbf{h} configures the energy landscape and the fields ψ evolve on it; (2) the *metriplectic spectrum*, where task complexity determines which channels of the dynamics to activate—from pure dissipation (Poisson equation) to full Hamiltonian-dissipative coupling; (3) the *Noether readout*, where the stress-energy tensor provides the feature extraction from evolved fields.

The architecture has not been tested at transformer scale, and significant open questions remain—notably whether symplectic integrators can stabilize deeper dynamics, and whether a single architecture can span all four domains. The consistent parameter efficiency across diverse tasks, however, indicates that physical structure encoded at the level of the architecture primitive can substantially reduce the capacity needed to solve a problem.

References

Ackley, D. H., Hinton, G. E., and Sejnowski, T. J. A learning algorithm for Boltzmann machines. *Cognitive Science*, 9(1):147–169, 1985.

- Agrawal, A., Amos, B., Barratt, S., Boyd, S., Diamond, S., and Kolter, J. Z. Differentiable convex optimization layers. In *Advances in Neural Information Processing Systems*, 2019.
- Alon, U. and Yahav, E. On the bottleneck of graph neural networks and its practical implications. In *International Conference on Learning Representations*, 2021.
- Amos, B. and Kolter, J. Z. OptNet: Differentiable optimization as a layer in neural networks. In *International Conference on Machine Learning*, 2017.
- Arnol'd, V. I. *Mathematical Methods of Classical Mechanics*. Springer-Verlag, 2nd edition, 1989.
- Bahdanau, D., Cho, K., and Bengio, Y. Neural machine translation by jointly learning to align and translate. In *International Conference on Learning Representations*, 2015.
- Bai, S., Kolter, J. Z., and Koltun, V. Deep equilibrium models. In *Advances in Neural Information Processing Systems*, 2019.
- Battaglia, P. W., Hamrick, J. B., Bapst, V., et al. Relational inductive biases, deep learning, and graph networks. *arXiv preprint arXiv:1806.01261*, 2018.
- Blelloch, G. E. Prefix sums and their applications. Technical Report CMU-CS-90-190, Carnegie Mellon University, 1990.
- Brandstetter, J., Hesselink, R., van der Pol, E., Bekkers, E., and Welling, M. Message passing neural PDE solvers. In *International Conference on Learning Representations*, 2022.
- Briggs, W. L., Henson, V. E., and McCormick, S. F. *A Multigrid Tutorial*. SIAM, 2nd edition, 2000.
- Bronstein, M. M., Bruna, J., Cohen, T., and Veličković, P. Geometric deep learning: Grids, groups, graphs, geodesics, and gauges. *arXiv preprint arXiv:2104.13478*, 2021.
- Brown, T., Mann, B., Ryder, N., et al. Language models are few-shot learners. In *Advances in Neural Information Processing Systems*, 2020.
- Bruna, J., Zaremba, W., Szlam, A., and LeCun, Y. Spectral networks and locally connected networks on graphs. In *International Conference on Learning Representations*, 2014.
- Chen, R. T. Q., Rubanova, Y., Bettencourt, J., and Duvenaud, D. Neural ordinary differential equations. In *Advances in Neural Information Processing Systems*, 2018.
- Chung, F. R. K. *Spectral Graph Theory*. AMS, 1997.
- Cohen, T. and Welling, M. Group equivariant convolutional networks. In *International Conference on Machine Learning*, 2016.
- Cranmer, M., Greydanus, S., Hoyer, S., Battaglia, P., Spergel, D., and Ho, S. Lagrangian neural networks. In *ICLR Workshop on Integration of Deep Neural Models and Differential Equations*, 2020.
- Cubuk, E. D., Zoph, B., Mane, D., Vasudevan, V., and Le, Q. V. AutoAugment: Learning augmentation policies from data. In *IEEE/CVF Conference on Computer Vision and Pattern Recognition*, 2019.
- Dao, T. and Gu, A. Transformers are SSMS: Generalized models and efficient algorithms through structured state space duality. In *International Conference on Machine Learning*, 2024.
- Defferrard, M., Bresson, X., and Vandergheynst, P. Convolutional neural networks on graphs with fast localized spectral filtering. In *Advances in Neural Information Processing Systems*, 2016.
- Desai, S. A., Mattheakis, M., Joy, H., Protopapas, P., and Roberts, S. J. Port-Hamiltonian neural networks for learning explicit time-dependent dynamical systems. *Physical Review E*, 104(3):034312, 2021.
- Devlin, J., Chang, M.-W., Lee, K., and Toutanova, K. BERT: Pre-training of deep bidirectional transformers for language understanding. In *Conference of the North American Chapter of the ACL*, 2019.

- Doran, C. and Lasenby, A. *Geometric Algebra for Physicists*. Cambridge University Press, 2003.
- Dosovitskiy, A., Beyer, L., Kolesnikov, A., et al. An image is worth 16x16 words: Transformers for image recognition at scale. In *International Conference on Learning Representations*, 2021.
- Du, W., Zhang, H., Du, Y., Meng, Q., Chen, W., Zheng, N., Shao, B., and Liu, T.-Y. SE(3) equivariant graph neural networks with complete local frames. In *International Conference on Machine Learning*, 2022.
- Elfwing, S., Uchibe, E., and Doya, K. Sigmoid-weighted linear units for neural network function approximation in reinforcement learning. *Neural Networks*, 107:3–11, 2018.
- Felgenhauer, B. and Jarvis, F. Mathematics of Sudoku I. *Mathematical Spectrum*, 39(1):15–22, 2006.
- Förstner, W. A feature based correspondence algorithm for image matching. *International Archives of Photogrammetry and Remote Sensing*, 26(3):150–166, 1986.
- Galimberti, C., Xu, L., and Ferrari-Trecate, G. Hamiltonian deep neural networks guaranteeing non-vanishing gradients by design. *IEEE Transactions on Automatic Control*, 68(5):3155–3162, 2023.
- Gilmer, J., Schoenholz, S. S., Riley, P. F., Vinyals, O., and Dahl, G. E. Neural message passing for quantum chemistry. In *International Conference on Machine Learning*, 2017.
- Greydanus, S., Dzamba, M., and Yosinski, J. Hamiltonian neural networks. In *Advances in Neural Information Processing Systems*, 2019.
- Grmela, M. and Öttinger, H. C. Dynamics and thermodynamics of complex fluids. I. Development of a general formalism. *Physical Review E*, 56(6):6620–6632, 1997.
- Gu, A., Goel, K., and Ré, C. Efficiently modeling long sequences with structured state spaces. In *International Conference on Learning Representations*, 2022.
- Gu, A. and Dao, T. Mamba: Linear-time sequence modeling with selective state spaces. In *International Conference on Machine Learning*, 2024.
- Hackbusch, W. *Multi-Grid Methods and Applications*. Springer-Verlag, 1985.
- Harris, C. and Stephens, M. A combined corner and edge detector. In *Alvey Vision Conference*, pp. 147–151, 1988.
- Ho, J., Jain, A., and Abbeel, P. Denoising diffusion probabilistic models. In *Advances in Neural Information Processing Systems*, 2020.
- He, K., Zhang, X., Ren, S., and Sun, J. Deep residual learning for image recognition. In *IEEE Conference on Computer Vision and Pattern Recognition*, 2016.
- He, J. and Xu, J. MgNet: A unified framework of multigrid and convolutional neural network. *Science China Mathematics*, 62(7):1331–1354, 2019.
- Hestenes, D. *Clifford Algebra to Geometric Calculus: A Unified Language for Mathematics and Physics*. D. Reidel Publishing, 1984.
- Hestenes, M. R. and Stiefel, E. Methods of conjugate gradients for solving linear systems. *J. Research National Bureau of Standards*, 49(6):409–436, 1952.
- Hinton, G. E. and Sejnowski, T. J. Boltzmann machines: Constraint satisfaction networks that learn. Technical Report CMU-CS-84-119, Carnegie Mellon University, 1984.
- Hopfield, J. J. Neural networks and physical systems with emergent collective computational abilities. *Proc. National Academy of Sciences*, 79(8):2554–2558, 1982.
- Huang, G., Sun, Y., Liu, Z., Sedra, D., and Weinberger, K. Q. Deep networks with stochastic depth. In *European Conference on Computer Vision*, pp. 646–661, 2016.

- Huang, G., Liu, Z., van der Maaten, L., and Weinberger, K. Q. Densely connected convolutional networks. In *IEEE/CVF Conference on Computer Vision and Pattern Recognition*, 2017.
- Ibarz, B., Kurin, V., Papamakarios, G., et al. A generalist neural algorithmic learner. In *Learning on Graphs Conference*, 2022.
- Ji, Z. CliffordNet: All you need is geometric algebra. *arXiv preprint arXiv:2601.06793*, 2026.
- Ioffe, S. and Szegedy, C. Batch normalization: Accelerating deep network training by reducing internal covariate shift. In *ICML*, 2015.
- Kadanoff, L. P. Scaling laws for Ising models near T_c . *Physics*, 2(6):263–272, 1966.
- Karniadakis, G. E., Kevrekidis, I. G., Lu, L., Perdikaris, P., Wang, S., and Yang, L. Physics-informed machine learning. *Nature Reviews Physics*, 3(6):422–440, 2021.
- Kingma, D. P. and Ba, J. Adam: A method for stochastic optimization. In *International Conference on Learning Representations*, 2015.
- Kipf, T. N. and Welling, M. Semi-supervised classification with graph convolutional networks. In *International Conference on Learning Representations*, 2017.
- Kirkpatrick, S., Gelatt, C. D., and Vecchi, M. P. Optimization by simulated annealing. *Science*, 220(4598):671–680, 1983.
- LeCun, Y. A tutorial on energy-based learning. In *Predicting Structured Data*. MIT Press, 2006.
- Li, G., Müller, M., Thabet, A., and Ghanem, B. DeepGCNs: Can GCNs go as deep as CNNs? In *International Conference on Computer Vision*, 2019.
- Li, Z., Kovachki, N., Aizzadenesheli, K., et al. Fourier neural operator for parametric partial differential equations. In *International Conference on Learning Representations*, 2021.
- Lieb, E. H. and Robinson, D. W. The finite group velocity of quantum spin systems. *Communications in Mathematical Physics*, 28(3):251–257, 1972.
- Lipman, Y., Chen, R. T. Q., Ben-Hamu, H., Nickel, M., and Le, M. Flow matching for generative modeling. In *International Conference on Learning Representations*, 2023.
- Liu, Z., Lin, Y., Cao, Y., et al. Swin transformer: Hierarchical vision transformer using shifted windows. In *International Conference on Computer Vision*, 2021.
- Liu, Z., Mao, H., Wu, C.-Y., Feichtenhofer, C., Darrell, T., and Xie, S. A ConvNet for the 2020s. In *IEEE/CVF Conference on Computer Vision and Pattern Recognition*, 2022.
- Liu, X., Gong, C., and Liu, Q. Flow straight and fast: Learning to generate and transfer data with rectified flow. In *International Conference on Learning Representations*, 2023.
- Liu, Z., Wang, Y., Vaidya, S., Rühle, F., Halverson, J., Soljačić, M., Hou, T. Y., and Tegmark, M. KAN: Kolmogorov-Arnold networks. In *International Conference on Learning Representations*, 2025.
- Lu, L., Jin, P., Pang, G., Zhang, Z., and Karniadakis, G. E. Learning nonlinear operators via DeepONet. *Nature Machine Intelligence*, 3(3):218–229, 2021.
- Marsden, J. E. and Ratiu, T. S. *Introduction to Mechanics and Symmetry*. Springer-Verlag, 2nd edition, 1999.
- Matsakis, N. D. and Klock, F. S. The Rust language. In *ACM SIGAda Ada Letters*, 34(3):103–104, 2014.
- Morrison, P. J. Hamiltonian description of the ideal fluid. *Reviews of Modern Physics*, 70(2):467–521, 1998.
- Nachtergaele, B. and Sims, R. Lieb-Robinson bounds and the exponential clustering theorem. *Communications in Mathematical Physics*, 265(1):119–130, 2006.

- Noether, E. Invariante Variationsprobleme. *Nachrichten von der Gesellschaft der Wissenschaften zu Göttingen, Mathematisch-Physikalische Klasse*, pp. 235–257, 1918.
- Olver, P. J. *Applications of Lie Groups to Differential Equations*. Springer-Verlag, 2nd edition, 1993.
- Onsager, L. Reciprocal relations in irreversible processes. I. *Physical Review*, 37(4):405–426, 1931.
- Öttinger, H. C. *Beyond Equilibrium Thermodynamics*. Wiley-Interscience, 2005.
- Palm, R., Paquet, U., and Winther, O. Recurrent relational networks. In *Advances in Neural Information Processing Systems*, 2018.
- Penedo, G., Kydlíček, H., Lozhkov, A., Mitchell, M., Colin, C., Mou, G., Ponferrada, E. G., Wolf, T., and Thrusch, T. The FineWeb datasets: Decanting the web for the finest text data at scale. *arXiv preprint arXiv:2406.17557*, 2024.
- Peng, B., Alcaide, E., Anthony, Q., Albalak, A., Arcadinho, S., Cao, H., Cheng, X., Chung, M., Grella, M., et al. RWKV: Reinventing RNNs for the transformer era. In *Findings of the Association for Computational Linguistics: EMNLP*, 2023.
- Pfaff, T., Fortunato, M., Sanchez-Gonzalez, A., and Battaglia, P. Learning mesh-based simulation with graph networks. In *International Conference on Learning Representations*, 2021.
- Raissi, M., Perdikaris, P., and Karniadakis, G. E. Physics-informed neural networks. *Journal of Computational Physics*, 378:686–707, 2019.
- Ramsauer, H., Schäfl, B., Lehner, J., et al. Hopfield networks is all you need. In *International Conference on Learning Representations*, 2021.
- Ronneberger, O., Fischer, P., and Brox, T. U-Net: Convolutional networks for biomedical image segmentation. In *MICCAI*, 2015.
- Sanchez-Gonzalez, A., Godwin, J., Pfaff, T., Ying, R., Leskovec, J., and Battaglia, P. Learning to simulate complex physics with graph networks. In *International Conference on Machine Learning*, 2020.
- Satorras, V. G., Hoogeboom, E., and Welling, M. E(n) equivariant graph neural networks. In *International Conference on Machine Learning*, 2021.
- Scarselli, F., Gori, M., Tsoi, A. C., Hagenbuchner, M., and Monfardini, G. The graph neural network model. *IEEE Transactions on Neural Networks*, 20(1):61–80, 2009.
- Scellier, B. and Bengio, Y. Equilibrium propagation: Bridging the gap between energy-based models and backpropagation. *Frontiers in Computational Neuroscience*, 11:24, 2017.
- Shewchuk, J. R. An introduction to the conjugate gradient method without the agonizing pain. Technical report, Carnegie Mellon University, 1994.
- Smolensky, P. Information processing in dynamical systems: Foundations of harmony theory. In *Parallel Distributed Processing*, Vol. 1. MIT Press, 1986.
- Song, Y., Sohl-Dickstein, J., Kingma, D. P., Kumar, A., Ermon, S., and Poole, B. Score-based generative modeling through stochastic differential equations. In *International Conference on Learning Representations*, 2021.
- Spielman, D. A. Spectral graph theory and its applications. In *IEEE Symposium on Foundations of Computer Science*, 2007.
- Tang, H., Huang, Z., Gu, J., Lu, B.-L., and Su, H. Towards scale-invariant graph-related problem solving by iterative homogeneous GNNs. In *Advances in Neural Information Processing Systems*, 2020.
- Thomas, N., Smidt, T., Kearnes, S., Yang, L., Li, L., Kober, K., and Riley, P. Tensor field networks: Rotation- and translation-equivariant neural networks for 3D point clouds. *arXiv preprint arXiv:1802.08219*, 2018.

- Topping, J., Di Giovanni, F., Chamberlain, B. P., Dong, X., and Bronstein, M. M. Understanding over-squashing and bottlenecks on graphs via curvature. In *International Conference on Learning Representations*, 2022.
- Toth, P., Rezende, D. J., Jaegle, A., Racanière, S., Botev, A., and Higgins, I. Hamiltonian generative networks. In *International Conference on Learning Representations*, 2020.
- Touvron, H., Lavril, T., Izacard, G., et al. LLaMA: Open and efficient foundation language models. *arXiv preprint arXiv:2302.13971*, 2023.
- Trottenberg, U., Oosterlee, C. W., and Schüller, A. *Multigrid*. Academic Press, 2001.
- Vaswani, A., Shazeer, N., Parmar, N., Uszkoreit, J., Jones, L., Gomez, A. N., Kaiser, L., and Polosukhin, I. Attention is all you need. In *Advances in Neural Information Processing Systems*, 2017.
- Veličković, P., Cucurull, G., Casanova, A., Romero, A., Liò, P., and Bengio, Y. Graph attention networks. In *International Conference on Learning Representations*, 2018.
- Veličković, P., Buesing, L., Overlan, M., et al. The CLRS algorithmic reasoning benchmark. In *International Conference on Machine Learning*, 2022.
- Veličković, P. and Blundell, C. Neural algorithmic reasoning. *Patterns*, 2(7):100273, 2021.
- Vlastelica, M., Paulus, A., Musil, V., Martius, G., and Rolinek, M. Differentiation of blackbox combinatorial solvers. In *International Conference on Learning Representations*, 2020.
- Wang, P.-W., Donti, P., Wilder, B., and Kolter, J. Z. SATNet: Bridging deep learning and logical reasoning using a differentiable satisfiability solver. In *International Conference on Machine Learning*, 2019.
- Wei, J., Wang, X., Schuurmans, D., et al. Chain-of-thought prompting elicits reasoning in large language models. In *Advances in Neural Information Processing Systems*, 2022.
- Weiler, M. and Cesa, G. General E(2)-equivariant steerable CNNs. In *Advances in Neural Information Processing Systems*, 2019.
- Winston, E. and Kolter, J. Z. Monotone operator equilibrium networks. In *Advances in Neural Information Processing Systems*, 2020.
- Wilson, K. G. and Kogut, J. The renormalization group and the ϵ expansion. *Physics Reports*, 12(2):75–199, 1974.
- Wu, Z., Pan, S., Chen, F., Long, G., Zhang, C., and Yu, P. S. A comprehensive survey on graph neural networks. *IEEE Transactions on Neural Networks and Learning Systems*, 32(1):4–24, 2020.
- Xu, K., Hu, W., Leskovec, J., and Jegelka, S. How powerful are graph neural networks? In *International Conference on Learning Representations*, 2019.
- Xu, Y., Liu, Z., Tegmark, M., and Jaakkola, T. Poisson flow generative models. In *Advances in Neural Information Processing Systems*, 2022.
- Ying, R., You, J., Morris, C., Ren, X., Hamilton, W. L., and Leskovec, J. Hierarchical graph representation learning with differentiable pooling. In *Advances in Neural Information Processing Systems*, 2018.
- Yato, T. and Seta, T. Complexity and completeness of finding another solution and its application to puzzles. *IEICE Transactions on Fundamentals*, E86-A(5):1052–1060, 2003.
- Yun, C., Bhojanapalli, S., Rawat, A. S., Reddi, S. J., and Kumar, S. Are transformers universal approximators of sequence-to-sequence functions? In *International Conference on Learning Representations*, 2020.

Zagoruyko, S. and Komodakis, N. Wide residual networks. In *British Machine Vision Conference*, 2016.

Zhang, J., Li, Z., and Chen, F. Neural logic machines for Sudoku solving. *arXiv preprint arXiv:2108.06455*, 2021.

Zhong, Y. D., Dey, B., and Chakraborty, A. Symplectic ODE-Net: Learning Hamiltonian dynamics with control. In *International Conference on Learning Representations*, 2020.

A Implicit Differentiation

Given $\boldsymbol{\psi}^* = A^{-1}\mathbf{b}$ where $A = L_W + \Lambda$ and downstream loss \mathcal{L} :

$$\frac{\partial \mathcal{L}}{\partial \mathbf{b}} = A^{-1} \frac{\partial \mathcal{L}}{\partial \boldsymbol{\psi}^*} = \mathbf{v}, \quad (21)$$

$$\frac{\partial \mathcal{L}}{\partial w_{ij}} = -\mathbf{v}_i(\boldsymbol{\psi}_i^* - \boldsymbol{\psi}_j^*) - \mathbf{v}_j(\boldsymbol{\psi}_j^* - \boldsymbol{\psi}_i^*), \quad (22)$$

where $\mathbf{v} = A^{-1}(\partial \mathcal{L} / \partial \boldsymbol{\psi}^*)$ is the adjoint variable. The same CG solver is reused for both forward and adjoint solves, requiring $O(N)$ total memory.

B Dirichlet Energy Derivation

Setting $\nabla_{\boldsymbol{\psi}} \mathcal{E}_{\text{Dir}} = 0$ from Eq. (9):

$$\sum_{j \in \mathcal{N}(i)} w_{ij}(\boldsymbol{\psi}_i - \boldsymbol{\psi}_j) + \Lambda_i \boldsymbol{\psi}_i = b_i \implies (L_W + \Lambda)\boldsymbol{\psi} = \mathbf{b}. \quad (23)$$

Since $L_W + \Lambda$ is SPD (Proposition 2), this is the unique global minimum.

C Lie Algebra of the Poisson Bracket

The Poisson bracket on the space of observables defines a Lie algebra. For the K -field system with Poisson tensor J_{ab} , the bracket of two observables $F(\boldsymbol{\psi})$ and $G(\boldsymbol{\psi})$ is:

$$\{F, G\}_J = \sum_{a,b} \frac{\partial F}{\partial \boldsymbol{\psi}_a} J_{ab} \frac{\partial G}{\partial \boldsymbol{\psi}_b}. \quad (24)$$

Skew-symmetry. Since $J_{ab} = -J_{ba}$, we have $\{F, G\} = -\{G, F\}$ directly.

Jacobi identity. For the finite-dimensional Poisson tensor used in Metriplector (J is a learned skew-symmetric matrix, constant in $\boldsymbol{\psi}$), the Jacobi identity $\{F, \{G, H\}\} + \{G, \{H, F\}\} + \{H, \{F, G\}\} = 0$ holds automatically because J has zero curvature (it is a constant-coefficient Poisson structure). For $\boldsymbol{\psi}$ -dependent J , the Jacobi identity imposes non-trivial constraints on the dependence [Marsden & Ratiu, 1999]. In the current architecture, J is parameterised as a learned skew-symmetric matrix (independent of $\boldsymbol{\psi}$), so the Jacobi identity is satisfied by construction.

Casimir invariants. A function $C(\boldsymbol{\psi})$ is a Casimir invariant of the Poisson bracket if $\{C, F\} = 0$ for *all* observables F , which requires $\sum_b J_{ab} \frac{\partial C}{\partial \boldsymbol{\psi}_b} = 0$ for all a . For a constant skew-symmetric J of rank $2r < K$, the Casimir space has dimension $K - 2r$. These Casimirs represent quantities that are conserved by *any* Hamiltonian—they are topological invariants of the phase space foliation. In Metriplector, the learned J typically has rank close to K (for even K), yielding few or no non-trivial Casimirs; the conservation guarantees come instead from energy conservation $dH/dt = 0$ along the Hamiltonian flow.

D Noether Currents for the Stress-Energy Readout

We derive the stress-energy tensor readout from Noether’s theorem for a system of K scalar fields on a 2D domain.

Lagrangian density. Consider the Lagrangian density:

$$\mathcal{L} = \frac{1}{2} \sum_{a=1}^K [(\partial_x \psi_a)^2 + (\partial_y \psi_a)^2] - V(\psi_1, \dots, \psi_K), \quad (25)$$

which describes K interacting scalar fields with gradient energy.

Translation invariance. Under a spatial translation $x^\mu \rightarrow x^\mu + \epsilon^\mu$ (with $\delta\psi_a = 0$), the Noether current is the canonical stress-energy tensor:

$$T^{\mu\nu} = \sum_{a=1}^K \frac{\partial \mathcal{L}}{\partial(\partial_\mu \psi_a)} \partial^\nu \psi_a - \eta^{\mu\nu} \mathcal{L} = \sum_{a=1}^K \partial^\mu \psi_a \cdot \partial^\nu \psi_a - \eta^{\mu\nu} \mathcal{L}. \quad (26)$$

The off-diagonal spatial components give the cross-field stress:

$$T_{ab}^{xy} = \partial_x \psi_a \cdot \partial_y \psi_b. \quad (27)$$

Decomposition into symmetric and antisymmetric parts. The tensor T_{ab}^{xy} decomposes as:

$$E_{ab} = \frac{1}{2}(T_{ab}^{xy} + T_{ba}^{xy}) = \frac{1}{2}(\partial_x \psi_a \partial_y \psi_b + \partial_x \psi_b \partial_y \psi_a), \quad (\text{energy density}) \quad (28)$$

$$V_{ab} = \frac{1}{2}(T_{ab}^{xy} - T_{ba}^{xy}) = \frac{1}{2}(\partial_x \psi_a \partial_y \psi_b - \partial_x \psi_b \partial_y \psi_a). \quad (\text{vorticity}) \quad (29)$$

The symmetric part E_{ab} measures co-located edge structure; the antisymmetric part V_{ab} measures rotational structure (corners, junctions). Together they yield K^2 independent features: K diagonal + $\binom{K}{2}$ cross-energy + $\binom{K}{2}$ vorticity.

Additional Noether currents. Rotational invariance ($x \rightarrow x \cos \theta - y \sin \theta$, $y \rightarrow x \sin \theta + y \cos \theta$) yields angular momentum:

$$L_a = x \cdot p_{y,a} - y \cdot p_{x,a}, \quad p_{\mu,a} = \psi_a \cdot \partial_\mu \psi_a. \quad (30)$$

Scale invariance ($x \rightarrow \lambda x$, $y \rightarrow \lambda y$) yields the dilation current:

$$D_a = x \cdot p_{x,a} + y \cdot p_{y,a}. \quad (31)$$

These position-dependent currents provide physics-native positional encoding without learned position embeddings.

E GENERIC Degeneracy Conditions

The GENERIC equation $\dot{z} = L\nabla E + M\nabla S$ requires two degeneracy conditions that prevent the two brackets from interfering:

Condition 1: $M \cdot \nabla E = 0$. The dissipative bracket cannot change the total energy. In Metriplector's dissipative branch, this is satisfied by construction: the Onsager matrix $M = L_W + \Lambda$ generates dynamics $\dot{\psi} = -M\psi + \mathbf{b}$ that minimise the Dirichlet energy $\mathcal{E} = \frac{1}{2}\psi^\top M\psi - \mathbf{b}^\top \psi$. At equilibrium ($\dot{\psi} = 0$), the energy is at its unique minimum. During evolution, $dE/dt = -\|\dot{\psi}\|_M^2 \leq 0$: energy is dissipated, not created.

Condition 2: $L \cdot \nabla S = 0$. The Hamiltonian bracket cannot produce entropy. For the Poisson bracket J with energy $E(\psi) = \frac{1}{2} \sum_a |\psi_a|^2$, the Hamiltonian flow $\dot{\psi}_a = \sum_b J_{ab} \psi_b$ satisfies $dE/dt = \psi^\top J \psi = 0$ by skew-symmetry of J . The entropy functional $S(\psi)$ (typically the negative Dirichlet energy in the dissipative branch) is likewise preserved: $dS/dt = \nabla S^\top J \nabla S = 0$.

Soft degeneracy in practice. In the full Metriplector architecture, the degeneracy conditions are not enforced exactly in each layer. Instead, they emerge approximately through training: the gradient signal rewards configurations where the Poisson bracket preserves important features (approximate energy conservation) and the dissipative bracket drives convergence (entropy increase). The architectural separation— J is skew-symmetric by construction, M is SPD by construction—guarantees the *structural* requirements ($J^\top = -J$, $M \succeq 0$) exactly, while the *functional* degeneracy ($M\nabla E = 0$, $L\nabla S = 0$) is approximately learned.